NJC

Accepted Manuscript

This is an *Accepted Manuscript*, which has been through the Royal Society of Chemistry peer review process and has been accepted for publication.

Accepted Manuscripts are published online shortly after acceptance, before technical editing, formatting and proof reading. Using this free service, authors can make their results available to the community, in citable form, before we publish the edited article. We will replace this *Accepted Manuscript* with the edited and formatted *Advance Article* as soon as it is available.

You can find more information about *Accepted Manuscripts* in the Information for Authors.

Please note that technical editing may introduce minor changes to the text and/or graphics, which may alter content. The journal's standard Terms & Conditions and the Ethical guidelines still apply. In no event shall the Royal Society of Chemistry be held responsible for any errors or omissions in this *Accepted Manuscript* or any consequences arising from the use of any information it contains.

ROYAL SOCIETY OF CHEMISTRY

www.rsc.org/njc

STRUCTURAL MODELING, *IN VITRO* ANTIPROLIFERATIVE ACTIVITY, AND EFFECT OF SUBSTITUENTS ON DNA FASTENING AND SCISSION ACTIONS OF HETEROLEPTIC COPPER(II) COMPLEXES WITH TERPYRIDINES AND NAPROXEN DRUG

Dharmasivam Mahendiran[a], Perumal Gurumoorthy[a], Krishnasamy Gunasekaran[b], Raju Senthil Kumar[c], Aziz Kalilur Rahiman[a*]

[a]*Post-Graduate and Research Department of Chemistry, The New College (Autonomous), Chennai-600 014, India*

[b]*CAS in Crystallograph and Bioinformatics, University of Madras, Guindy Campus, Chennai-600 025, India*

[c]*Department of Pharmaceutical Chemistry, Swami Vivekanandha College of Pharmacy, Elayampalayam, Tiruchengodu-637 205, India*

Abstract

A series of heteroleptic copper(II) complexes of the type [Cu($L^{1–6}$)(nap)Cl] (**1–6**) ($L^{1–6}$ = 4'–(4–substituted)–2,2':6',2''–terpyridines, nap = naproxen drug) have been synthesized and characterized. The single crystal analysis of complexes **1** and **6** show distorted octahedral geometry around copper(II) ion. Structural parameters from the crystallographic and DFT studies are in good agreement with each other. HOMO–LUMO energy levels are constructed and the corresponding theoretical frontier energy gaps are calculated to realise the charge transfer occurring in the molecule, and the lowering of HOMO–LUMO band gap supports bioactive property of the molecule. Electrochemical studies show one-electron irreversible reduction process in the cathodic potential (E_{pc}) region from –0.75 to –0.82 V. The obtained room temperature magnetic moment values (1.82–1.93 BM), XRD and EPR spectral data support distorted octahedral geometry for the copper(II) complexes. The binding studies of complexes **1**, **5** and **6** with CT–DNA imply groove mode of binding, and the complex **5** exhibits highest binding affinity than the other complexes. The binding results were further supported by molecular docking studies. The higher binding propensity of complex **5** containing **R5** was proved by computationally derived factors such as chemical potential (μ),

chemical hardness (η), electrophilicity (ω) and nuclease independent chemical shift (NICS). All the complexes display pronounced nuclease activity against supercoiled pBR322 DNA. *In vitro* antiproliferative activity of the complexes **1**, **5** and **6** against human breast cancer cells (MCF-7) were carried out by MTT assay, which shows the potent activity of **1** and **5** with lower IC_{50} values with respect to cisplatin and comparable to doxorubicin. The complexes induce mitochondrial-mediated and caspase-dependent apoptosis with increase in G_0-G_1 and subsequent arrest in the S phase, in cell cycle evolution.

Keywords: Heteroleptic complexes; Naproxen; DFT; DNA interaction; Antiproliferation; Cell cycle arrest.

*Corresponding author. Tel.: +91 44 2835 0297; Fax: +91 44 2835 2883.
E-mail address: akrahmanjkr@gmail.com

---

1. Introduction

The rigid side effects including ototoxicity, nephrotoxicity, myelotoxicity, peripheral, neuropathy and neurotoxicity, nausea, low water solubility and drug resistance of platinum based anticancer drugs has forced the researchers to develop effective anticancer drugs based on metals other than platinum [1]. Next to ruthenium, copper complexes are regarded as the most promising alternatives for cisplatin analogs [2, 3]. Copper is a bio-essential metal ion, and its complexes also known to play a significant role either in naturally occurring biological systems or as pharmacological agents. The biological processes like electron transfer, oxidation and dioxygen transport involve copper in their active sites [4]. The copper(II) complexes with tunable coordination geometries in a redox active environment could find better application at the cellular level, and treat with chronic diseases, also act as antioxidant, antimicrobial, antiparasitic, and antitumor agents [5–8].

In recent decades, tremendous interest has been devoted to complexes of the tri-hetero aromatic planar terpyridines in the area of bio-inorganic and medicinal chemistry due to their splendid complexing properties, geometric viewpoint, synthetic simplicity, catalytic behaviour, and in asymmetric catalysis, as well as eminent edifice blocks in both organic and inorganic supramolecular chemistry because of their π stacking competence [9–11]. The non-steroidal anti-inflammatory drugs (NSAIDs), which are among the most frequently prescribed drugs in modern medicine have exhibited chemopreventive and anti–tumorigenic activity by reducing the number and size of carcinogen–induced colon tumors and exhibiting a synergistic role on the activity of certain antitumor drugs [12]. Naproxen is one of the most important enantiomeric pure compound, where the (*S*)-enantiomer is the active ingredient in an anti-inflammatory drug, while the (*R*)-enantiomer is a liver toxin. The (*S*)-enantiomer naproxen is utilized for anti-inflammatory and analgesic effects in the symptomatic treatment of rheumatoid arthritis, osteoarthritis, juvenile rheumatoid arthritis, ankylosing spondylitis, arthritic pain and bleeding [13].

The non-steroidal anti-inflammatory drugs (NSAIDs) with copper(II) complexes were shown better activity than free drug and exhibit a lower toxicity than inorganic forms of copper [14]. Heteroleptic copper(II) complexes of terpyridines and bidentate/tridentate ligands, which interact with DNA effectively and also exhibit antitumor activity against human lung cancer cell line A549, have been reported [15]. To the best of our knowledge, the antiproliferative activity, cell cycle arrest and DFT studies of naproxen based copper(II) complexes and their derivatives are scare in literature [16, 17], and also there is a lack of systematic studies of their characterization and antiproliferative studies. Therefore, the modern research was focused to develop the novel heteroleptic copper(II) complexes of terpyridines and NSAIDs.

In view of all these observations, we have been interested in exploring the biological efficacy of heteroleptic copper(II) complexes of 4'–(4–substituted)–2,2':6',2''–terpyridines and NSAID drug, sodium naproxen. A host of methods like absorption, viscosity, cyclic voltammetry and electrophoresis techniques have been used to probe the DNA interaction of the copper(II) complexes. Cytotoxicity of the complexes was tested against human breast cancer cell line (MCF-7) using MTT assay. Apoptotic cell death was further evidenced from flow cytometry assay. Further, an in-depth theoretical understanding of the geometries on DFT and HOMO-LUMO analysis was performed in order to elucidate information regarding electrophilicity (ω), hardness (η), chemical potential (μ) and nucleus independent chemical shift (NICS) calculations using the Gaussian 03 program.

2. Results and discussion

2.1 Design and synthesis of the complexes

The heteroleptic copper(II) complexes (**1–6**) were synthesized in high yield by the reaction of 4'–(4–substituted)–2,2':6',2''–terpyridines (R–tpy) with $CuCl_2.2H_2O$ in the presence of NSAID drug sodium naproxen ($C_{13}H_{13}O$–COO^- Na^+) in methanol (**Scheme 1**). The authenticities of the complexes were assigned by elemental analysis, FT–IR, absorption, ESI-MS and EPR spectral methods along with single crystal XRD.

In the IR spectrum, the disappearance of broad band at 3356 cm^{-1} due to –OH stretching of naproxen carboxylic group can be ascribed to presence of covalent bond between copper and $–COO^-$ of naproxen. The carbonyl stretching vibration of naproxen (1728 cm^{-1}) was shifted to lower frequency (1604–1621 cm^{-1}) in the complexes, which indicate the coordination of naproxen to metal ion through carbonyl oxygen. The characteristic band of carbonyl group, i.e. υ(COO) asymmetric and symmetric vibrations, observed as strong absorption band at 1631 and 1346 cm^{-1} in naproxen, also shifted to 1556–1564 and 1370–1398 cm^{-1}, respectively, in metal complexes. The difference $\Delta\upsilon = \upsilon_{asym}$

(C=O) − υ_{sym} (C=O), is a useful characteristic for determining the coordination mode of the carboxylato ligands. The Δ values are less than 200 cm^{-1}, indicating a bi-dentate coordination mode of the carboxylato group of naproxen [18]. The mass spectra of all the complexes were studied in positive mode, which confirm the formation of heteroleptic copper(II) complexes. **Fig. S1** depicts the mass spectrum of complex **6** that shows molecular ion peak at m/z = 592 due to the absence of chlorine atom $[CuL^6(nap)]^+$, which is equivalent of its molecular weight. The base peak at m/z 399 denotes $[CuL^6]^+$. The mass spectral results are in good agreement with the proposed molecular formulae of the complexes.

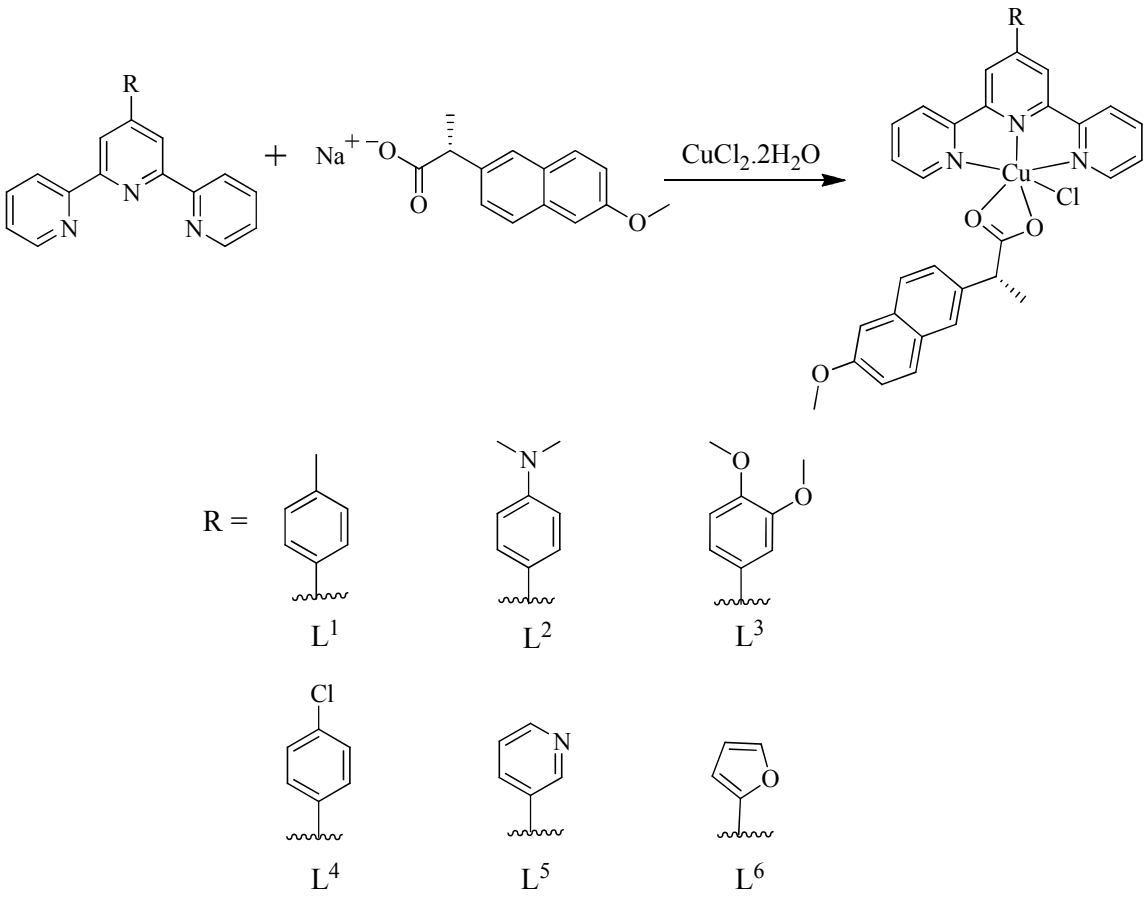

Scheme 1 General scheme for the synthesis of heteroleptic copper(II) complexes (**1**–**6**).

The UV-Vis absorption spectra of complexes (**1**−**6**) were recorded in DMF medium, which gain the valid information about the structural properties of the complexes. A strong

band obtained in the range 265–276 nm is due to an intra-ligand charge transfer transition (π–π*), while moderately intense band appeared in the range 337–358 nm may be due to charge transfer from the naproxen oxygen to Cu(II) ion. All the complexes show a broad band in the range 612–624 nm due to metal centred d–d transition, which suggest distorted octahedral geometry around the copper(II) ion [19, 20].

The diffuse reflectance spectroscopy has been used for estimating the width of the energy gap using Kubelka–Munk (K–M) model [21]. A graph is plotted between $[F(R)h\upsilon]^2$ and hυ, the intercept value is the band gap energy (**Fig. S2)**. The spectra of complexes **1** and **5** show broad absorption band at 265 and 271 nm (4.67, 4.56 eV), and another small band at 615 and 620 nm (2.02, 2.00 eV), respectively, and the liquid UV-Vis absorption spectra of complexes **1** and **5** reveals a band gap of 271, 610 nm (4.56, 2.03 eV) and 275, 616 nm (4.50, 2.01 eV), respectively. The similar pattern obtained in UV-Vis spectra of the complexes in solid and solution implies that the octahedral geometries of complexes, as evidenced by the X-ray crystal structures of complexes **1** and **6**, is retained in solution.

2.2 Structural description of [Cu(L^1)(nap)Cl] (1)

Suitable single crystals of green coloured copper(II) complex **1** was obtained by slow evaporation of the reaction mixture for several days, which crystallizes as **1**·CH_3OH. The crystal data and structure refinement parameters are listed in **Table 1**, and the details of hydrogen bonding parameter are given in **Table 2**. The crystal belongs to monoclinic primitive space group *P21* with two molecules in the asymmetric unit along with two lattice methanol molecules. The crystal structure has been determined and refined to the final R factor of 0.0995. The ORTEP diagram with 30% thermal ellipsoid of one molecule is shown in **Fig 1**, in which the lattice methanol molecules are omitted for clarity. In both molecules of the asymmetric unit, the preference for octahedral coordination is witnessed in **Table 3**. **Fig. S3** represents molecular packing viewed down "a" axis where the methanol mediated

hydrogen bonding are exhibited. The average coordination distance of the second carboxyl oxygen to Cu(II) is 2.959 Å. O8 makes bifurcated hydrogen bonds with C16 and C19 (–x+2, +y+1/2, –z+2) with donor-acceptor distances of 3.402(1) Å & 3.345(1) Å and angles of 175.3(1) & 171.4(1), respectively. The other hydrogen bonds are O7-H7A...O2, [2.822(1) Å, 156.39], O8-H8...O6 [2.612(1) Å, 163.11] and C3-H3...Cl1 [3.506(1) Å, 136.29]. The phenyl ring attached with terpyridine maintains co-planarity.

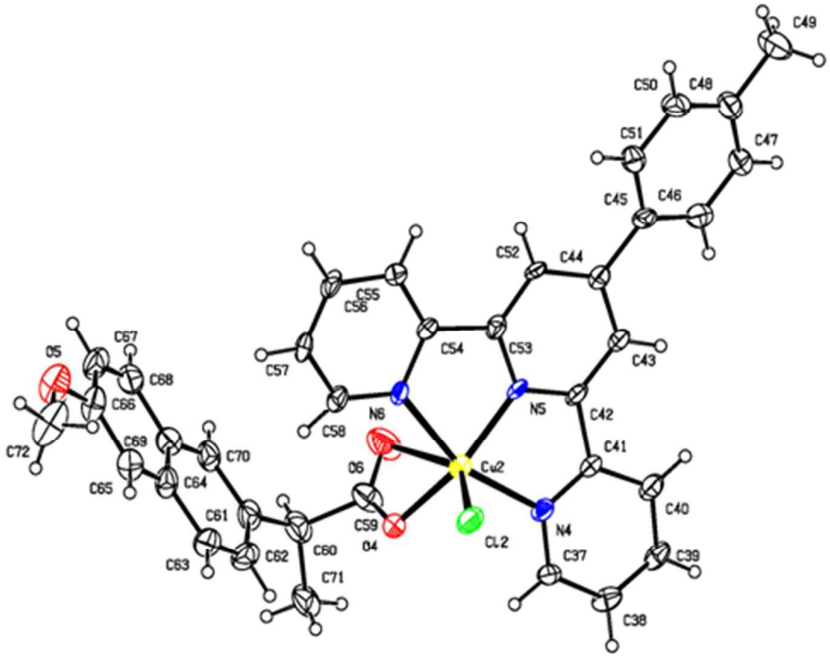

Fig. 1 The ORTEP diagram of one molecule of complex **1**·CH_3OH drawn with 30% thermal ellipsoid. The lattice methanol molecules are omitted for clarity.

Table 1 Crystal data and structure refinement for complexes **1** and **6**

Complex	**1**·CH_3OH	**6**·H_2O·1/2CH_3OH
CCDC	1021393	1033741
Empirical formula	$C_{37}H_{34}ClCuN_3O_4$	$C_{67}H_{60}Cl_2Cu_2N_6O_{11}$
Formula weight	683.66	1323.19
Temperature (K)	293 (2)	293 (2)
Wavelength (Å)	0.71073	0.71073
Crystal system	Monoclinic	Triclinic
Space group	*P21*	*P1*
a (Å)	8.6469(7)	8.590(5)
b (Å)	34.562(3)	10.579(5)
c (Å)	11.4333(10)	18.094(5)
α (°)	90.00	83.522(5)
β (°)	109.165(5)	84.936(5)
γ (°)	90.00	69.681(5)
Volume (Å^3)	3227.5(5)	1530.0(12)
Z	4	1
Calculated density (Mg m^{-3})	1.406	1.436
Absorption coefficient (mm^{-3})	0.805	0.850
F(000)	1418	684
Crystal size (mm)	0.30 × 0.25 × 0.20	0.30 × 0.20 × 0.20
θ range for data collection (°)	1.18 – 25.0	2.05 – 26.98
Reflections collected	11264	11558
Independent reflections	7717	8814
Refinement method	Full–matrix–least squares on F^2	Full–matrix–least squares on F^2
Data/restrains/parameters	7717/269/838	8814/7/815
GOF on F^2	1.106	0.987
R_{int}	0.0824	0.0374
Final R indices [$I > 2\sigma(I)$]	0.0995	0.0406
R indices (all data)	0.1408	0.0598

Table 2 Hydrogen bonding parameters for complex **1**·CH_3OH [Å and °].

D-H...A	d(D-H)	d(H...A)	d(D...A)	<(DHA)
O(7)-H(7A)...O(2)	0.82	2.05	2.82(2)	156
O(8)-H(8)...O(6)	0.82	1.82	2.61(2)	163
C(3)-H(4)...Cl(1)$^{1\#}$	0.93	2.77	3.51(3)	136
C(4)-H(4)...Cl(2)$^{3\#}$	0.93	2.75	3.64(2)	163
C(16)-H(16)..O(8)$^{5\#}$	0.93	2.48	3.40(2)	175
C(19)-H(19)...O(8)$^{5\#}$	0.93	2.42	3.35(4)	171
C(20)-H(20)...O(7)$^{2\#}$	0.93	2.58	3.35(4)	139
C(39)-H(39)...O(8)$^{2\#}$	0.93	2.58	3.39(2)	146
C(40)-H(40)...O(7)$^{4\#}$	0.93	2.56	3.49(3)	177
C(43)-H(43)..O(7)$^{4\#}$	0.93	2.59	3.51(3)	177
C(55)-H(55)...Cl(1)$^{3\#}$	0.93	2.70	3.571(18)	156
C(56)-H(56)...Cl(2)$^{1\#}$	0.93	2.82	3.511(19)	133

Symmetry transformations used to generate equivalent atoms:
#1 -1+x,y,z; #2 1+x,y,z; #3 1-x,-1/2+y,1-z; #4 1-x,1/2+y,1-z; #5 2-x,-1/2+y,2-z;
#6 2-x,1/2+y,2-z

Table 3 The coordination shell around the metal ion in complexes **1** and **6**

L...M	Distance (Å)	L…M	Distance (Å)
Complex **1**·CH_3OH			
N1–Cu1	2.087(10)	N4–Cu2	2.059(9)
N2–Cu1	1.939(10)	N5–Cu2	1.924(10)
N3–Cu1	2.080(10)	N6–Cu2	2.036(9)
O1–Cu1	1.948(10)	O4–Cu2	1.977(9)
O2–Cu1	3.022	O6–Cu2	2.896
Cl1–Cu1	2.427(4)	Cl2–Cu2	2.406(4)
Complex **6**·H_2O·1/2CH_3OH			
N1–Cu1	2.035(5)	N11–Cu2	2.030(5)
N2–Cu1	1.945(3)	N12–Cu2	1.920(4)
N3–Cu1	2.060(4)	N13–Cu2	2.030(4)
O2–Cu1	1.925(4)	O6–Cu2	1.923(4)
Cl1–Cu1	2.518(2)	Cl2–Cu2	2.515(2)
O3–Cu1	2.778(5)	O7–Cu2	2.685(5)

2.3 Structural description of [Cu(L^6)(nap)Cl] (6)

Suitable single crystals of green coloured copper(II) complex **6** was obtained by slow evaporation of the reaction mixture for several days, which crystallizes as **6**·H_2O·1/2CH_3OH. The crystal data and structure refinement parameters are listed in **Table 1**, and the details of hydrogen bonding parameter are given in **Table 4**. The crystal belongs to triclinic primitive space group *P1* with two coordination complexes in the asymmetric unit along with two lattice water molecules but only one lattice methanol molecule common for both the asymmetric units. The crystal structure has been determined and refined to the final R factor of 0.0406. The ORTEP diagram with 30% thermal ellipsoid of one molecule is shown in **Fig 2**. In both molecules of the asymmetric unit, the preference for octahedral coordination is witnessed as shown in **Table 3**. Due to the bi-dentating nature of the carboxylic group and partially because of the bulkiness of the ligand (naproxen), which prevented the approach of a free ligand such as water, a distorted octahedral geometry is observed. The coordination distance of Cu–N ranges from 1.92 Å to 2.06 Å. The Cu–Cl average coordination length is 2.51 Å. The Cl–Cu–O (second carboxyl oxygen) is around 150°, which is deviated from 180°. With torsion angles C3–C4–C5–C6 [13.9(10)°] and O1–C4–C5–C6 [–161.7(5)°], the furan ring maintains near co-planarity with the terpyridine moiety to which it is attached. The methoxy group of naproxen maintains co-planarity with naphthalene by torsion angles C27–C28–O4–C33 = –176.5(6) & C29–C28–O4–C33 = 1.4(8)°. **Fig. 3** represents molecular packing viewed down 'a' axis where the water mediated hydrogen bonding chains are exhibited. One of the water molecules make strong hydrogen bonds, which bridges the bounded chlorine and the carboxyl second ligating centre in turn makes its coordination weaker (with the average (among two structures) distance of 2.731 Å). The details are O2W-H2WB …O3; O2W...O3 (x+1,+y,+z) = 2.726(7) Å & O2W-H2WB...O3 = 158.7 (2.4)°;

O2W-H2WA …Cl1; O2W...Cl1 (x+1,+y+1,+z) = 3.253(5) Å & O2W-H2WA...Cl1 = 148.2 (1.7)°.

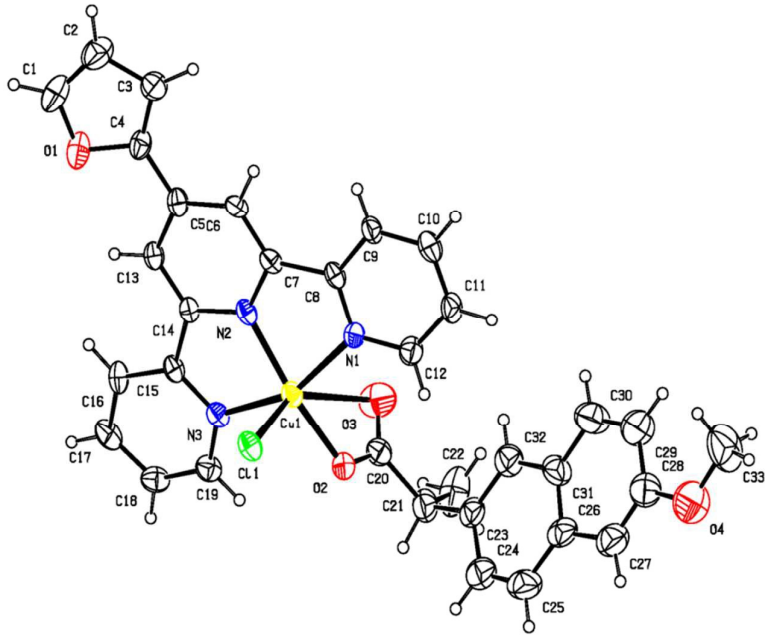

Fig. 2 The ORTEP diagram of one molecule of complex **6**·H_2O·1/2CH_3OH drawn with 30% thermal ellipsoid. The lattice water and methanol molecules are omitted for clarity.

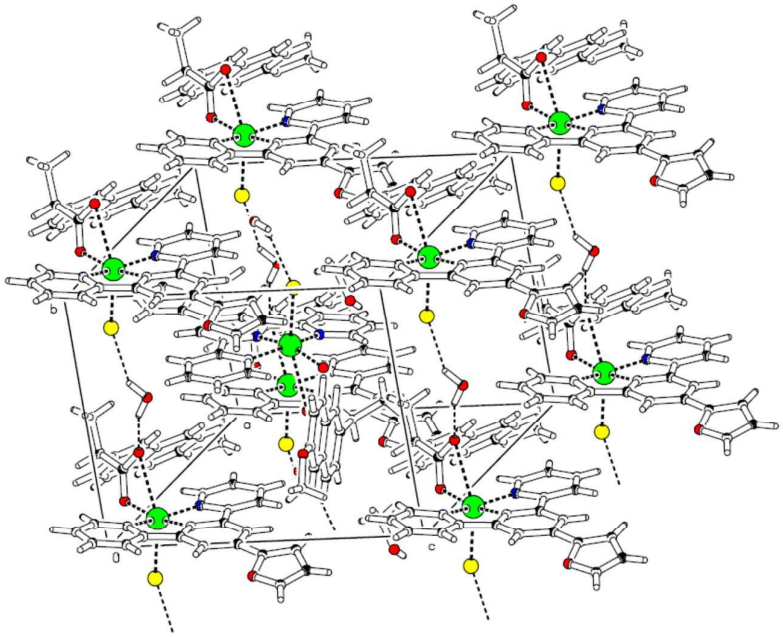

Fig. 3 Unit cell packing diagram of complex **6**·H_2O·1/2CH_3OH viewed down "a" axis (One of the lattice water make chains of hydrogen bonding runs along 'b axis' by bridging the bounded chlorine and the second carboxyl oxygen).

Table 4 Hydrogen bonding parameters for complex **6**·H_2O·1/2CH_3OH [Å and °]

D-H...A	d(D-H)	d(H...A)	d(D...A)	<(DHA)
C(6)-H(6)...O(1W)	0.93	2.58	3.166(11)	121.7
C(6)-H(6)...Cl(2)$^{\#1}$	0.93	2.88	3.789(8)	166.0
C(9)-H(9)...Cl(2)$^{\#1}$	0.93	2.91	3.804(9)	162.2
C(11)-H(11)...Cl(1)$^{\#2}$	0.93	2.82	3.506(9)	131.7
C(36)-H(36)...Cl(1)$^{\#3}$	0.93	2.83	3.710(10)	157.7
C(39)-H(39)...Cl(1)$^{\#3}$	0.93	2.81	3.723(8)	168.5
C(42)-H(42)...Cl(1)$^{\#3}$	0.93	2.86	3.759(8)	162.7
C(44)-H(44)...Cl(2)$^{\#4}$	0.93	2.92	3.583(8)	129.1
C(49)-H(49)...O(2W)	0.93	2.57	3.413(10)	151.0
O(9)-H(9A)...Cl(2)$^{\#5}$	0.82	2.44	3.191(10)	152.1
O(1W)-H(1WB)...Cl(2)$^{\#1}$	0.98(3)	2.90(7)	3.195(8)	98(5)
O(2W)-H(2WA)...Cl(1)$^{\#6}$	0.96(3)	2.37(3)	3.260(6)	156(5)
O(2W)-H(2WB)...O(3)$^{\#2}$	0.94(3)	1.90(4)	2.720(9)	144(5)
C(6)-H(6)...O(1W)	0.93	2.58	3.166(11)	121.7
C(6)-H(6)...Cl(2)$^{\#1}$	0.93	2.88	3.789(8)	166.0
C(9)-H(9)...Cl(2)$^{\#1}$	0.93	2.91	3.804(9)	162.2
C(11)-H(11)...Cl(1)$^{\#2}$	0.93	2.82	3.506(9)	131.7
C(36)-H(36)...Cl(1)$^{\#3}$	0.93	2.83	3.710(10)	157.7
C(39)-H(39)...Cl(1)$^{\#3}$	0.93	2.81	3.723(8)	168.5
C(42)-H(42)...Cl(1)$^{\#3}$	0.93	2.86	3.759(8)	162.7
C(44)-H(44)...Cl(2)$^{\#4}$	0.93	2.92	3.583(8)	129.1
C(49)-H(49)...O(2W)	0.93	2.57	3.413(10)	151.0
O(9)-H(9A)...Cl(2)$^{\#5}$	0.82	2.44	3.191(10)	152.1
O(1W)-H(1WB)...Cl(2)$^{\#1}$	0.98(3)	2.90(7)	3.195(8)	98(5)
O(2W)-H(2WA)...Cl(1)$^{\#6}$	0.96(3)	2.37(3)	3.260(6)	156(5)
O(2W)-H(2WB)...O(3)$^{\#2}$	0.94(3)	1.90(4)	2.720(9)	144(5)

Symmetry transformations used to generate equivalent atoms:
#1 x,y-1,z; #2 x+1,y,z; #3 x,y+1,z; #4 x-1,y,z; #5 x-1,y-1,z; #6 x+1,y+1,z

2.4 Frontier molecular orbital properties

Since the crucial electronic excitations occur from the highest occupied molecular orbitals (HOMOs) to the lowest unoccupied molecular orbitals (LUMOs), it is important to form efficient charge-separated states with the HOMOs localized on the donor subunit and the LUMOs on the acceptor subunit. The HOMO–LUMO helps to characterize the chemical reactivity and kinetic stability of the molecule and also excellent indicators of electron transport in molecular systems. [22]. A molecule with a small gap is more polarized and is known as soft molecule. The lowering of the HOMO−LUMO band gap is essentially a consequence of the large stabilization of the LUMO due to the strong electron-accepting ability of the electron-acceptor group.

The molecular orbital energies and the HOMO–LUMO gaps of complex **1** is depicted in **Fig. S4**. The bond lengths and bond angles of complexes **1**, **2**, **5** and **6** derived from DFT calculations are presented in **Table S1**. For complexes **1** and **6**, the comparison of bond lengths and angles between calculated and X-ray structure shows an ample agreement. Interestingly, the terpyridine ligands play significant role in the virtual frontier and in the lower occupied molecular orbitals in both complexes **1** and **6** (see section 1 of ESI for details). The orbital energy level analysis for complexes **1**, **5** and **6** showed that E_{HOMO} values are –4.01 eV, –2.28 and –3.84 eV, respectively while E_{LUMO} values are –1.81 eV, –0.51 and –1.64 eV, respectively (**Fig. S5**). As a result, **1** is better electron donor and **5** is better electron acceptor. The ΔE values of complexes **1** (2. 20 eV), **5** (1.77 eV) and **6** (2.20 eV) calculated at the DFT level reflects the higher stability of **5** compared to other complexes. Additionally, the observed lower orbital gap indicates the eventual charge transfer taking place within the molecule and the obtained low energy gap supports bioefficacy of the complexes. Literature reports have also indicated that frontier molecular orbitals are very important to investigate the trend in DNA-binding of complexes and their spectral properties [23]. The calculated

HOMO–LUMO energy gap agree reasonably with experimentally obtained HOMO–LUMO energy gap through liquid and solid absorption spectra (**Table S2**).

2.5 EPR investigation

The EPR signal taken from powdered complexes are shown in **Fig. S6**. The obtained effective magnetic moment (μ_{eff}) values of complexes (1.82–1.93 BM) is slightly higher than the spin only value (1.73 BM), which is due to the monomeric nature of complexes and there is no possibility of an exchange interaction. These values are typical for mononuclear copper(II) compounds having d^9 electronic configuration. The X-band EPR spectra show isotropic character and does not contain any hyperfine lines. The observed values show $g_{\|} > g_{\perp}$, which indicates the presence of unpaired electron in the $d_{x^2-y^2}$ orbital of the copper(II) ion, giving $^2B_{1g}$ as the ground state [24]. The $g_{\|}$ and $g_{\perp}$ values of six coordinated complexes were closer to 2 ($g_{\|} > g_{\perp}$), which suggests major distortion from octahedral symmetry in the copper(II) complexes [25]. These observations were further supported by the crystal structure. The geometric parameter, $G = (g_{\|}-2)/(g_{\perp}-2)$, for axial spectra measures the exchange interaction between copper(II) centers in the polycrystalline state. If $G > 4.0$, the exchange interaction is negligible, and if it is less than 4.0 considerable exchange interaction is indicated. In the percent cases, the G values lie in the range 1.8–2.0, indicating the presence of considerable interaction between the copper centres.

2.6 Electrochemistry

All the complexes show a molar conductance in the range 13–19 $\Omega^{-1}\,cm^2\,M^{-1}$ which indicates the non-electrolytic nature of the complexes [26]. The redox properties of complexes (**1**–**6**) have been investigated by cyclic voltammetry in the potential range –0.4 to –1.6 V in DMF containing 0.1 M tetra(*n*-butyl)ammonium perchlorate. Cyclic voltammograms with different scan rates show no corresponding anodic peak in the reverse direction, which indicates the irreversible electron process, and the complexes exhibit a well defined one

electron transfer reduction waves (**Fig. S7**) assigned to the $Cu^{II} \rightarrow Cu^{I}$ reduction at the reduction peak potential (**Table S3**). The irreversible nature of the redox wave clearly shows that the reorganizational barrier during the redox process is large in all cases. The reduction potential of complex **4** is less negative relative to other complexes, which indicates that the +1 oxidation state is more stabilized in complex **4** than the other complexes.

2.7 Stability of the complexes

The stability of complexes in aqueous solution over a prolonged period of time is an essential requirement for drug preparation. It is postulated that many organometallic complexes lack stability under conditions in which living organisms thrive [27], therefore we decided to test the stability of synthesized complexes in aqueous solution using a UV-Vis spectrophotometer. The measurements were executed over different time intervals during 24, 48 and 72 h using a scanning kinetic program (**Fig. S8**). The UV–Vis spectra recorded directly after dilution of the tested complexes **1**, **5** and **6**, and after 24 and 48 h did not show any differences, while the 72 h samples show negligible differences, which indicate the stability of the complexes in aqueous solution.

2.8 DNA binding studies

2.8.1 Electronic absorption studies

In general, metal complexes can bind to DNA *via* covalent (base binding) and/or non covalent interactions like intercalation, electrostatic, and binding along major (or) minor groove. The binding ability of the complexes (**1**, **5** and **6**) with CT–DNA was determined by keeping the complex at fixed concentration and varying the concentration of DNA solution, during which an increase in absorption intensities (hyperchromic effect) was observed in the intra-ligand region (**Fig. 4**). These spectral characteristic suggest that the complexes bind either to the external contact (electrostatic binding) or to the major/minor grooves of DNA. The observed 'hyperchromic effect' results from the structural damage of DNA, is indicative

of strong binding of the complexes to CT–DNA. However, there was practically absence of any shift in the absorption bands of the complexes in the presence of DNA, which strongly suggest the groove binding mode of the complexes to DNA. The DNA possess several hydrogen bonding sites, which are accessible both in the major and minor grooves [28]. This groove binding results in structural reorganization of CT–DNA, which entails partial unwinding or damage of the double helix at the exterior of phosphate backbone leading to the formation of a cavity to accommodate the complex. Consequently, uptake occurs with partial melting of the double helix and generation of an appropriate binding pocket [29]. Analysis of the spectral data in the presence of DNA gave binding constant K_b, of 2.38 ± 0.17, 4.27 ± 0.19 and 2.24 ± 0.25 × 10^5 M^{-1} for complexes **1**, **5** and **6**, respectively (**Table 5**). From the binding constant values, it is clear that the complexes are moderate binders and complex **5** shows the highest binding affinity amongst them, because it has H-bonding capabilities and hence may be involved in secondary H-bonding interaction with DNA. Interestingly, the binding strength of complexes are higher than that of related terpyridine [18, 30–32] and NSAIDs based complexes [33] or the effective anticancer drug cisplatin (3.20 ± 0.15 = 10^4 M^{-1}) [34], but lower than the classical intercalator ethidium bromide, in which the binding constants have been formed to be in the order of 10^6–10^7 M^{-1} [35].

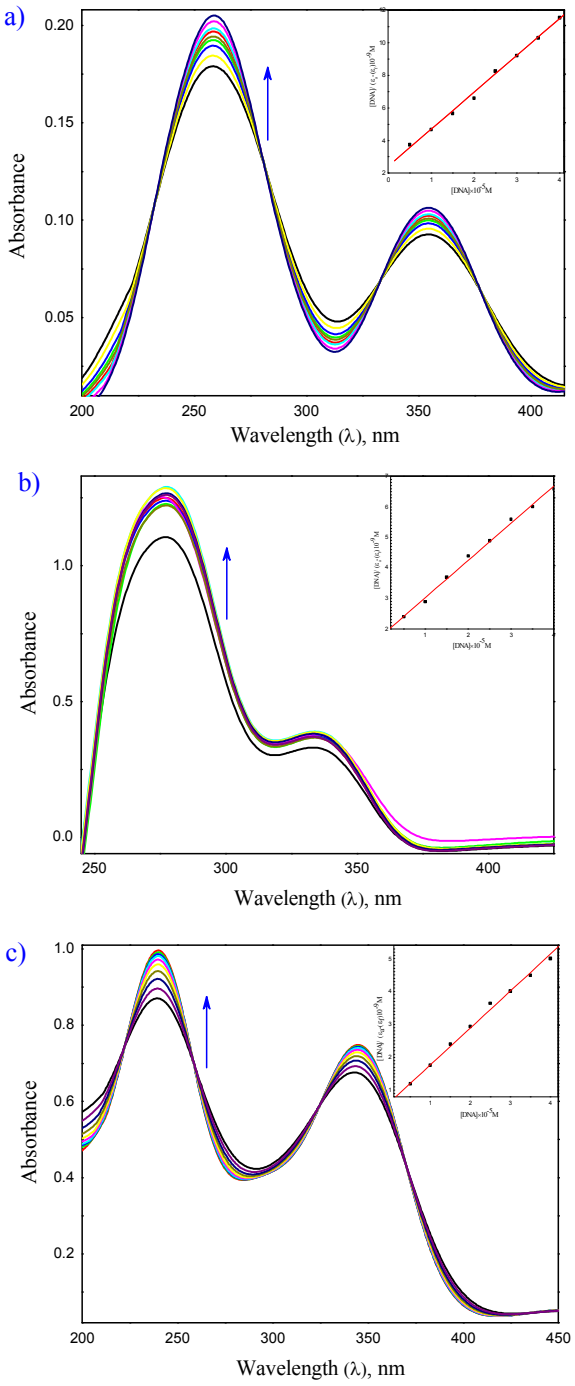

Fig. 4 Absorption spectra of complexes **1** (a), **5** (b) and **6** (c) (25 μM) in Tris–HCl buffer upon addition of CT–DNA (0–5 μM). Arrows indicate the change in absorbance upon increasing the DNA concentration. Inset: plots of [DNA]/(ε_a – ε_f) *versus* [DNA] for the titration of DNA with complexes.

Table 5 DNA-binding constants (K_b), Molecular docking parameters and IC_{50} values of complexes **1**, **5** and **6** against MCF-7 cancer cell line

Complexes	$K_b \times 10^5$ (M^{-1})	Free energy of binding kcal mol^{-1}	IC_{50} values (μM)
1	2.38 ± 0.17	–5.12	11.51 ± 0.15
5	4.27 ± 0.19	–5.76	10.40 ± 0.3
6	2.24 ± 0.25	–4.77	31.03 ± 1.2
Cisplatin	0.32 ± 0.02	-	28.03
Doxorubicin	-	-	10.90

2.8.2 Thermal denaturation studies

Thermal denaturation studies can conveniently be used in predicting the nature of binding of the complexes to DNA and their relative binding strength. A high ΔT_m value is suggestive of an intercalative mode of binding of the metal complex to DNA, while a low value (1–3 °C) indicates a groove and/or electrostatic binding mode [35]. The double stranded DNA tends to gradually dissociate to single strands on increase in the solution temperature and generates a hyperchromic effect on the absorption spectra of DNA bases (λ_{max} = 260 nm). DNA (100 μM) melting experiments revealed that T_m of CT–DNA is 61.0 °C in the absence of the complex (**Fig. 5**). Upon addition of complexes **1**, **5** and **6** **(**25 μM**)** T_m increased to 61.5 ± 1°C, 62.1 ± 1°C and 62.8 ± 1.5 °C, respectively. The small change in T_m is indicative of the fact that binding of the complex with DNA is not very strong. Complexes **1**, **5** and **6** have comparatively lower ΔT_m values, ranging from 0.5 to 1.8 °C, indicating primarily DNA groove binding propensity of the complexes [36].

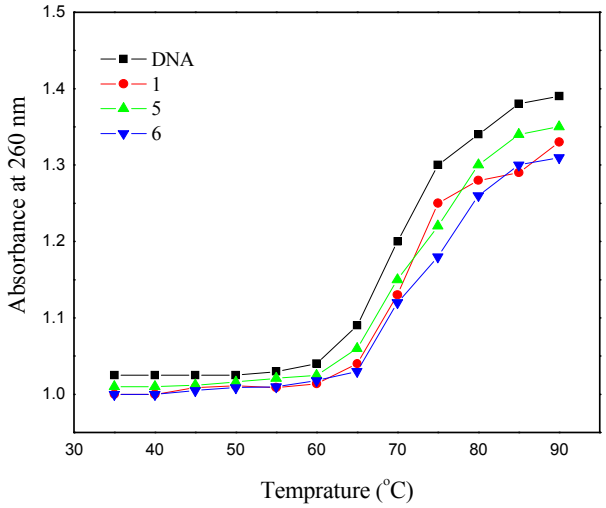

Fig. 5 Melting curves of CT–DNA (100 μM) upon addition of complexes **1**, **5** and **6** (25 μM).

2.8.3 Viscosity measurement studies

To further clarify the interaction mode of the complexes with DNA, viscosity measurements were carried out on CT–DNA by varying the concentration of the added complexes. The experiment involves the measurement of the flow rate of DNA solution through a capillary viscometer. A classical intercalative mode causes a significant increase in viscosity of DNA solution due to increase in separation of base pairs at intercalation sites and hence an increase in overall DNA length. By contrast, drug molecules that bind exclusively in the DNA grooves (e.g., netropsin, distamycin), under the same conditions, typically cause less pronounced (positive or negative) or no changes in DNA solution viscosity [37]. The plot of $(\eta/\eta_0)^{1/3}$ *versus* [Complex]/[DNA] gives a measure of the viscosity changes (**Fig. S9**). The obtained plots show only a minor change in the relative viscosity, which clearly indicates groove binding mode for complexes. Therefore, we can conclude that the complexes **1**, **5** and **6** bind to CT–DNA in the groove regions [38]. The binding ability of complexes to increase the viscosity of DNA follows the order **5** > **1** > **6**, which is in accordance with UV-Vis absorption spectral results.

2.8.4 Electrochemical titration

The electrochemical investigations of metal–DNA interactions can provide a useful complement to spectroscopic methods, e.g., for non-absorbing species, and yield information about interactions with both the reduced and oxidized form of the metal. In general, the electrochemical potential of a small molecule will shift positively when it intercalates into DNA double helix, and it will shift to a negative direction in the case of electrostatic interaction with DNA. Additionally, in the case of more than one potential, the positive shift of E_{P1} accompanied by a negative shift of E_{P2} may suggest the binding of the molecule to DNA by both intercalation and electrostatic interaction [39]. The cyclic voltammogram of complexes **1**, **5** and **6** in the absence and presence of CT–DNA were recorded in Tris–HCl/NaCl buffer solution (pH, 7.3) using tetra(*n*-butyl)ammonium perchlorate (TBAP) as supporting electrolyte at the scan rate of 100 mV/s in the potential range –1.6 to –0.4 V (**Fig. S10**). All the complexes exhibit same electrochemical behaviour upon addition of DNA, and for increasing amounts of DNA, the considerable decrease in voltammetric current (i_{pc} = 1.23 to 2.06) and negative shift (E_{pc} = –0.75 to –0.82 V) was observed (**Table S4**). Upon addition of DNA, the decrease in current and negative shift is higher for complex **5** than for other complexes, which suggest the stronger binding affinity and the binding affinity follows the order **5** > **1** > **6**. The decrease in current may be attributed to the diffusion of the complexes bound to the large, slowly diffusing DNA molecule and also decrease in current values are ascribed to the stronger binding between the complexes and DNA [40]. The electrochemical studies corroborated well with the spectral studies and thereby authenticate the strong interaction of CT–DNA with complexes.

2.8.5 EPR measurements

The EPR spectroscopy affords unique information on the DNA binding stereo-specificities and dynamics of many paramagnetic metal complexes, in particular those of Cu(II) complexes [41]. The EPR spectra of complexes **1** and **6** incubated with CT–DNA for 24 h, recorded in methanol solution are shown in **Fig. S11**. No significant changes was observed in the EPR spectra, which imply that those interactions occur mostly into the grooves of DNA (major or minor grooves), without noteworthy modifications in the copper ion environmental geometry [42].

2.8.6 Molecular docking with DNA

The rigid molecular docking (two interacting molecules were treated as rigid bodies) studies were performed to predict the binding modes of compounds with a DNA duplex of sequence d(CGCGAATTCGCG)$_2$ dodecamer (PDB ID:1BNA), and provide an energetically favourable docked structures (**Fig. 6**). It is evident from the studies that these complexes (**1**, **5** and **6**) fits into the major groove comfortably involving outside edge interactions without disrupting the double helical structure of DNA and stabilized by hydrogen bonding interaction and hydrophobic contacts with DNA functional groups which define the stability of groove and all the complexes interact closely with adenine unit of the DNA [43]. It is well known that the interactions of chemical species with the minor groove of B-DNA differ from those occurring in the major groove, both in terms of electrostatic potential and steric effects because of the narrow shape of the former. Small molecules interact with the minor groove, while large molecules tend to recognize the major groove-binding site [44]. The results of molecular docking show that the complexes **1**, **5** and **6** bind efficiently with the DNA receptor and exhibit free energy of binding (FEB) values –5.12, –5.76 and –4.77 kcal mol^{-1}, respectively. The more negative relative binding energy of complex **5** indicated its strong binding ability to the DNA than the complexes **1** and **6**. Because right handed DNA is

complementary to complex **5**, it exhibits strong interactions *via* symmetrical hydrogen bonding [45]. Thus, it can be concluded that the molecular docking studies provide additional evidence for the preferred major groove modes of binding with the copper(II) complexes.

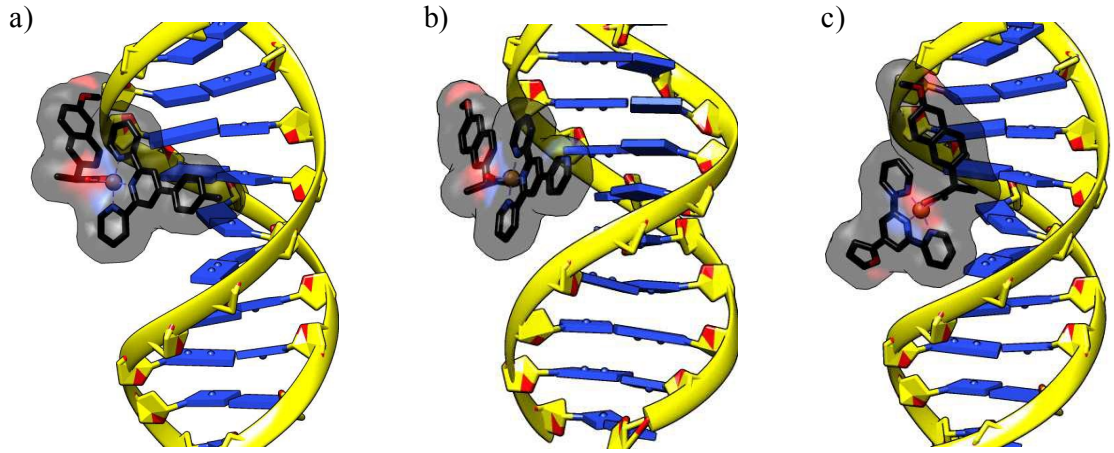

Fig. 6 Molecular docked model of complexes **1** (a), **5** (b) and **6** (c) with DNA (PDB ID: 1BNA) dodecamer duplex of sequence d(CGCGAATTCGCG)$_2$.

2.8.7 Effect of ligand substituents on DNA binding

To further clarify the influence of substituents on the binding constant values, computational studies were carried out for complexes **1**, **5** and **6** (**Fig. S12**), which differ only in their substituents (**R** group). Therefore, calculations were carried out by considering only the tolyl, pyridyl and furyl groups (**R1**, **R5** and **R6**, respectively) as representative of **1**, **5** and **6**, respectively. Density functional theory (DFT) based descriptors such as chemical potential (μ), chemical hardness (η), electrophilicity (ω) and nucleus independent chemical shift (NICS) are calculated at the centre of the rings [46–48]. The chemical hardness and softness of molecule is a good indicator of the chemical stability of a molecule. From the HOMO–LUMO energy gap, one can find whether the molecule is hard or soft. The molecules having large energy gap are known as hard and molecules having a small energy gap are known as soft molecules. The soft molecules are more polarizable than the hard ones because they need small energy for excitation. This four parameters μ, η, ω and NICS are measures of reactivity

and stability (**Table 6**). According to the maximum hardness principle (MHP), the most stable structure has the maximum hardness. Thus, the neat **R5** with maximum hardness are chemically more stable compared to the **R1** and **R6**. The complex **5** possess higher electrophilicity compared to **R1** and **R6**, indicating more reactivity of **R5** than **R1** and **R6**. Generally, systems with negative NICS values are aromatic, since negative values arise when diatropic ring current (shielding) dominates, whereas systems with positive values are antiaromatic because positive values arise when paratropic current (deshielding) dominates, and the more negative the NICS value, the more aromatic the system and higher the stability. The NICS value of **R5** is greater than that of **R1** and **R6**, indicating the higher reactivity and higher stability of **R5**. Thus, the pyridyl-substituted molecule (complex **5**) binds to DNA more strongly ($K_b = 4.27 \pm 0.19 \times 10^5$ M^{-1}) relative to the tolyl and furyl substituted molecules (complex **1** and **6** with K_b values of 2.38 ± 0.17 and $2.24 \pm 0.25 \times 10^5$ M^{-1}, respectively).

Table 6 Chemical potential (μ), chemical hardness (η), electrophilicity (ω) and nucleus independent chemical shift (NICS(0)) values calculated by using the B3LYP/6-31G* level of theory

Substituents	μ (eV)	η (eV)	ω (eV)	NICS (0) (ppm)
R1 (Toluene)	–3.13	3.27	1.49	–9.6
R5 (Pyridine)	–3.76	3.13	2.26	–17.9
R6 (Furan)	–2.78	3.32	1.16	–0.06

2.9 Gel electrophoresis

Hydrolytic cleavage of double stranded DNA involving a phosphodiester bond offers important advantages in the cellular processes in comparison to the oxidative DNA cleavage targeted at the deoxyribose sugar moiety or the guanine base. Small metal complexes that promote the hydrolytic cleavage of DNA could be useful for molecular biology and drug design. The principle of this method is that molecules migrate in the gel as a function of their

mass, charge and shape, with supercoiled DNA migrating faster than open circular molecules of the same mass and charge. When circular plasmid DNA is subject to electrophoresis, relatively fast migration is generally observed for the intact supercoiled form. When scission occurs on one strand (nicking), the supercoil (SC, Form I) relaxes to generate a slower-moving nicked circular (NC, Form II) form. When both strands are cleaved, a linear form (LC, Form III) is generated, which migrates between SC and NC forms of DNA. Mononuclear metal complexes designed for hydrolytic DNA cleavage have been reviewed in few excellent articles [49]. Terpyridine–based and also other copper(II) complexes, have been reported to bring about DNA cleavage even in the absence of any coreagent [50, 51], and thus the hydrolytic cleavage of present complexes **1**, **5** and **6** were examined on supercoiled plasmid pBR322 DNA to target the phosphor-diester linkages, deoxiribose sugar or nucleobases. The resulting DNA minor groove binder has been expected to exhibit efficient hydrolytic cleavage [51], and capable of promoting hydrolytic cleavage of DNA. Even in the presence of DMSO and sodium azide, which are quenchers of hydroxyl radicals and singlet oxygen, respectively, complexes were able to convert the supercoiled form of DNA to the nicked circular form of DNA (**Fig. 7**). The observed results show that the complexes were able to convert the supercoiled form to the nicked circular form of DNA without any additives, and capable of promoting hydrolytic cleavage of DNA. Complex **5** was found to be more efficient in bringing about hydrolytic cleavage of DNA compared to complexes **1** and **6**.

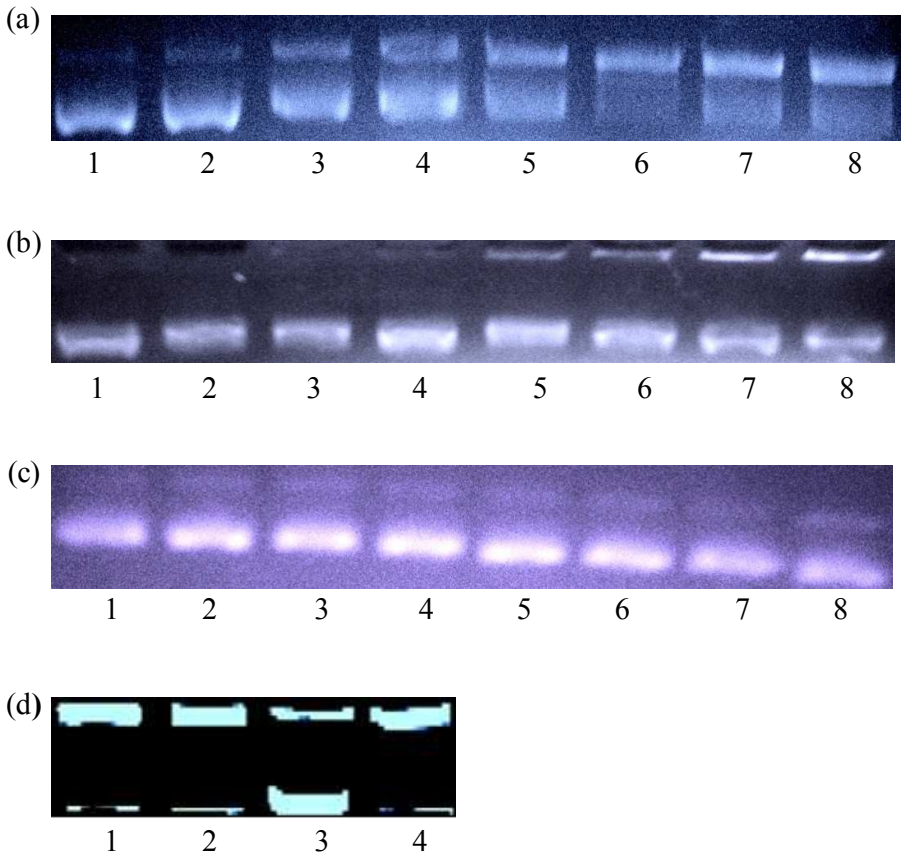

Fig. 7 Hydrolytic cleavage of pBR322 DNA (33.3 μM) by complexes **1** (a) **5** (b) and **6** (c) in Tris–HCl buffer. Lane 1, DNA alone; lane 2, DNA + **1**/**5**/**6** (25 μM); lane 3, DNA + **1**/**5**/**6** (50 μM); lane 4, DNA + **1**/**5**/**6** (100 μM); lane 5, DNA + **1**/**5**/**6** (150 μM); lane 6, DNA + **1**/**5**/**6** (200 μM); lane 7, DNA + **1**/**5**/**6** (250 μM); lane 8, DNA+ /**5**/**6** (300 μM). (d) Analysis of the capacity of T4 DNA ligase to relegate DNA cleaved by complex **5.** Lane 1, DNA + **5** (100 μM); Lane 2, DNA + **5** (100 μM) + DMSO (70 μM); Lane 3, NC obtained using **5** + T4 ligase; Lane 4, DNA + **5** (100 μM) + NaN_3 (50 μM).

Since the complex **5** was able to convert almost 90% of supercoiled DNA to the nicked circular form of DNA, and also with the increase in reaction time, the amount of Form II increased and Form I gradually decreased, indicating that the complex is involved in single-stand DNA cleavage. On the other hand under identical conditions, complexes **1** and **6** brought about only 20% and 10% conversion, respectively. To corroborate the hydrolytic nature of the scission process, we have conducted additional cleavage experiments by using

T4 ligase enzymatic assay [52], and the results show the relegation of nicked circular to supercoiled form (**Fig. 7d**). Further, the experiments also performed in the presence of the hydroxyl radical quencher DMSO and the singlet oxygen quencher sodium azide. From these observations, the addition of DMSO and NaN_3 does not show any inhibition (**Fig. 7d**, lanes 2 and 4), indicating the absence of hydroxyl radical and singlet-oxygen as ROS in the scission process.

2.10 Cytotoxicity studies

2.10.1 MTT assay

The antiproliferative properties of the complexes (**1**, **5** and **6**) have been evaluated against human breast cancer cell line (MCF-7) by MTT assay. The metabolic activity of the cells were assessed by their ability to cleave the tetrazolium rings of the pale yellow MTT and form a dark blue water-insoluble formazan crystal, only live cells reduce yellow MTT to blue formazan products but not dead cells. In the present antiproliferative analysis, various concentration (2, 5, 10, 25 and 50 μM) of copper(II) complexes were tested against MCF-7 cells for 24 h. The complex was dissolved in DMSO and a blank sample containing the same volume of DMSO was taken as a control to identify the activity of the solvent. In this study, cisplatin and doxorubicin were taken as reference standards. The cell viability was concentration-dependent (2–50 μM), with increasing the concentrations a decrease in cell viability was observed as shown in **Fig. 8**. The IC_{50} values were calculated from the numbers of cells that survived at each particular complex concentration after exposure for 24 h. The IC_{50} values of the complexes have been found to be 11.51 ± 0.15, 10.40 ± 0.3 and 31.03 ± 1.2 μM for **1**, **5** and **6**, respectively (**Table 5**). Further, as revealed by the observed IC_{50} values, the potency of complexes to kill cancerous cells follow the order **5** > **1** > **6**. Interestingly, the complex **5** showed highest anticancer activity against MCF-7 breast cancer cell line (IC_{50} = 10.40 ± 0.3 μM), which was more potent than positive control cisplatin with IC_{50} values of

28.03 μM. Subsequently, the IC_{50} value of **5** is almost equal to that of the standard anticancer drug doxorubicin (10.90 μM) against the same MCF-7 cells [53, 54]. Interestingly, the IC_{50} values are much lower than that for previously reported terpyridine based [55, 56], and other copper(II) complexes [57] against the same cell line MCF-7. The IC_{50} values indicating that the complexes have potential as an effective metal-based anticancer drug, possibly targeting DNA. Further investigation on the complexes is needed to establish their ability to act as anticancer drugs.

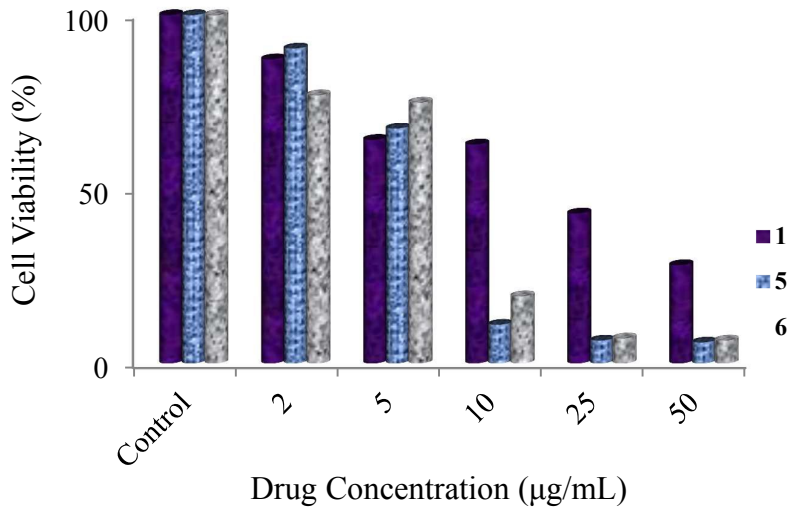

Fig. 8 Antiproliferative effect of complexes **1**, **5** and **6** on MCF-7 cells by MTT assay.

2.10.2 Effect of complexes 1 and 5 on apoptosis of MCF-7 cells

Apoptosis, or programmed cell death, is a highly conserved, tightly controlled cell suicide process that is regulated by many different intracellular and extracellular events to ablate neoplastic cells in normal physiological functions. Apoptosis is controlled by two potential pathways, the mitochondrial pathway and the death receptor pathway. The mitochondrial pathway is characterized by the loss of mitochondrial transmembrane potential and release of cytochrome *c* [58]. The death receptor pathway is mediated by serial activation of Fas [a cell surface death receptor of the tumor necrosis factor (TNF) family of cytokines].

Apoptosis is an intrinsic suicide serves to remove excess, damaged or infected cells in metazoans. Apoptosis was characterized by a variety of morphological and biochemical events, including phosphatidylserine (PS) externalization, chromatin condensation, genomic DNA fragmentation, and plasma-membrane blebbing [59, 60]. It occurs under physiological conditions such as tissue and organ development, tissue maintenance, and dysregulated apoptosis has been associated with autoimmune disease and cancer. Toxic stimuli capable of inducing apoptosis in susceptible cells include irradiation, DNA-damaging drugs, and activation of the Fas antigen [61–63]. The importance of understanding apoptosis is underscored further by the fact that the "therapeutic index" of different antineoplastic therapies may correlate with the differential capacity of tumor and normal cells to undergo apoptosis [64]. "Necrosis" is a form of cell death that differs from apoptosis [65]. Such death usually results from overwhelming damage to cells, leading to their death without the involvement of a genetically encoded suicide program [66].

In the present study, Hoechst fluorescence assay was employed to study the effect of complexes **1** and **5** on MCF-7 cell line. After treatment with the test compounds for 48 h, apoptosis was detected by observing the morphology of MCF-7 cells such as chromatin condensation and nuclear fragmentation. Among the compounds tested, complex **5** showed more activity when compared to complex **1**. The results are presented in **Table S5**. The morphological changes on MCF-7 cells at different concentration of test compounds are shown in **Fig. 9**. Condensed chromatin and fragmented nuclei could also be found in many treated cells, which are classic characteristics of apoptotic cells. Taken together, these data suggest that distinct stages of apoptosis can be identified by staining of cells with Hoechst. This assay should be useful for the detection and further characterization of cells at different stages in the apoptotic process. These results suggest that both the compounds may exert its

antitumor effects associated with two fundamental processes, suppression of cell proliferation and induction of apoptosis on human MCF-7 cells *in vitro*.

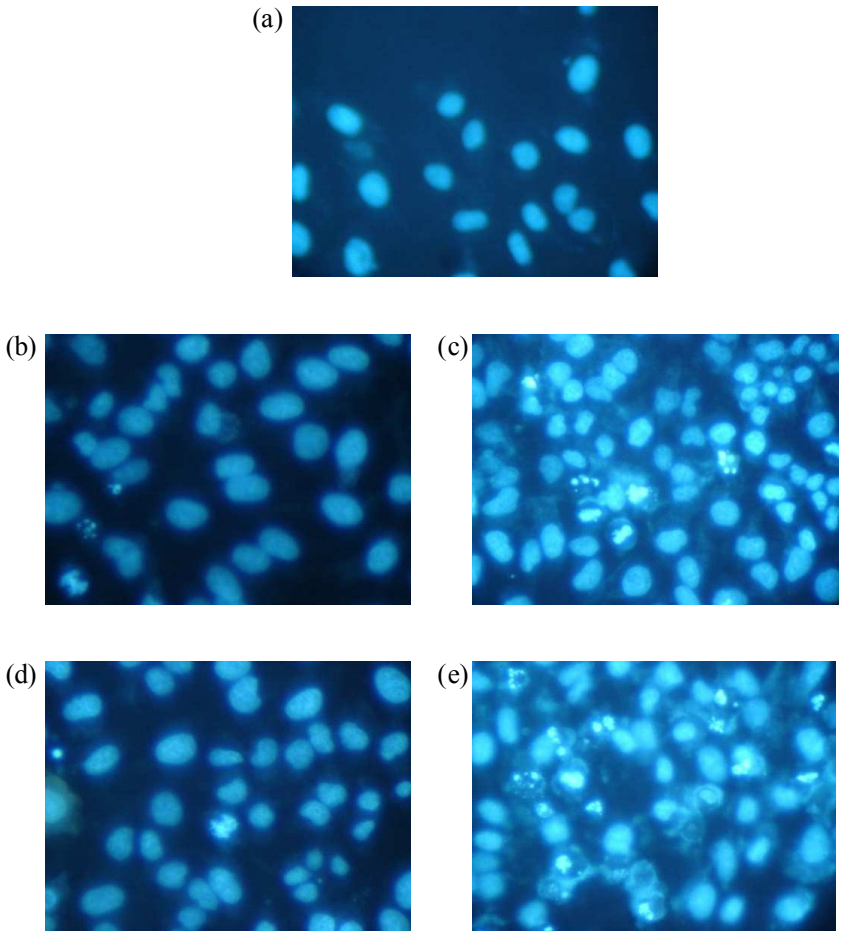

Fig. 9 Hoechst 33258 staining of MCF-7 cells for 24 h, control (a), complexes **1** (25 μM) (b), **1** (50 μM) (c), **5** (25 μM) (d) and **5** (50 μM) (e).

2.10.3 Cell apoptosis analysis by flow cytometry

Flow cytometry is one of the most powerful and specific method to investigate the molecular and morphological events occurring during cell death. Flow cytometry technique used various parameters including light diffraction i.e., forward scatter (FSC) and side scatter (SSC), and uptake of fluorescent dyes e.g., fluorescein isothiocyanate (FITC), phyco-erythrin (PE), CyChrome/RED613, propidium iodide (PI) and CyChrome fluorochromes are conjugated to antibodies that bind epitopes on the cell surface. Moreover, propidium iodide is

a vital dye that is excluded by live cells, which have intact plasma membranes; however, it enters dead cells and intercalates into DNA, thereby making it possible to distinguish live cells from dead cells and to quantitate the number of live cells in a particular sample [67]. Flow cytometry with PI staining is particularly valuable when coupled with staining by fluorochrome conjugated antibodies because the combination provides a means of quantitating live cells that have a certain surface phenotype within a heterogeneous cell population [68, 69]. In our present investigation, apoptosis was detected by flow cytometric analysis using propidium iodide staining, and the complexes were incubated for 24 h at a concentration of 25 μM. The measurement of PI binding to the cell surface as an indicator for apoptosis has to be performed along with a dye exclusion test, to establish the integrity of the cell membrane. The fractions of cell populations in different quadrants are analyzed using quadrant statistics. The upper left quadrant (Q1) contains dead cells; the lower left quadrant contains (Q3) healthy cells; the upper and lower right quadrants (Q2 and Q4) contain late apoptosis and early apoptosis cells, respectively. From this we can infer the apoptosis inducing potential of the complexes. The complexes induce apoptosis with different potencies, which is well in accordance with their *in vitro* cytotoxicities (**Fig. 10**). Since the result show that the percentage population of viable cells decreases while that in the fourth quadrant Q4 increases, indicating that complexes **1**, **5** and **6** trigger early apoptosis. Cisplatin, under similar experimental conditions was found to cause predominantly the early apoptotic mode of cellular death [70]. Among the complexes examined, the most dramatic impact on apoptosis was observed with complex **5**. After exposure to complex **5** at 25 μM for 24 h, apoptotic MCF-7 cells in early and late stages amount to 84% in total, with only 13% cells remaining viable.

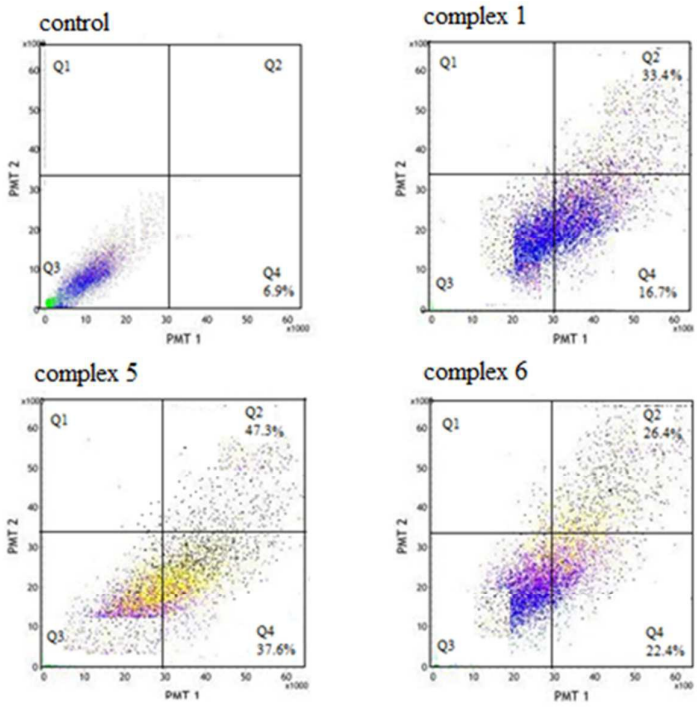

Fig. 10 Flow cytometric results after the exposure of MCF-7 cells to the complexes **1**, **5** and **6** (25 μM) for 24 h. Four areas in the diagrams represent four different cell states: necrotic cells (Q1), late apoptotic cells (Q2), living cells (Q3) and early apoptotic cells (Q4).

2.10.4 Cell cycle arrest

The quantitative analysis of cell cycle is very important in the study of molecular mechanism of cell death and cell cycle progression [71]. The blockades of cell cycle progress by anticancer agents prevent the proliferation of cancer cells, which is also exploited for cancer therapy. Flow cytometric analysis of cell cycle measures the apoptotic changes in cells by staining them with DNA dyes. Apoptotic cells, due to a change in membrane permeability, showed an increased up-take of the vital dye, PI, compared to live cells [72]. The status of the cell cycle profile and the mechanism of cell division and cell death induced by the complexes **1**, **5** and **6** on MCF–7 cells were analyzed (**Fig. 11**). Increase in the percentage of cells in the

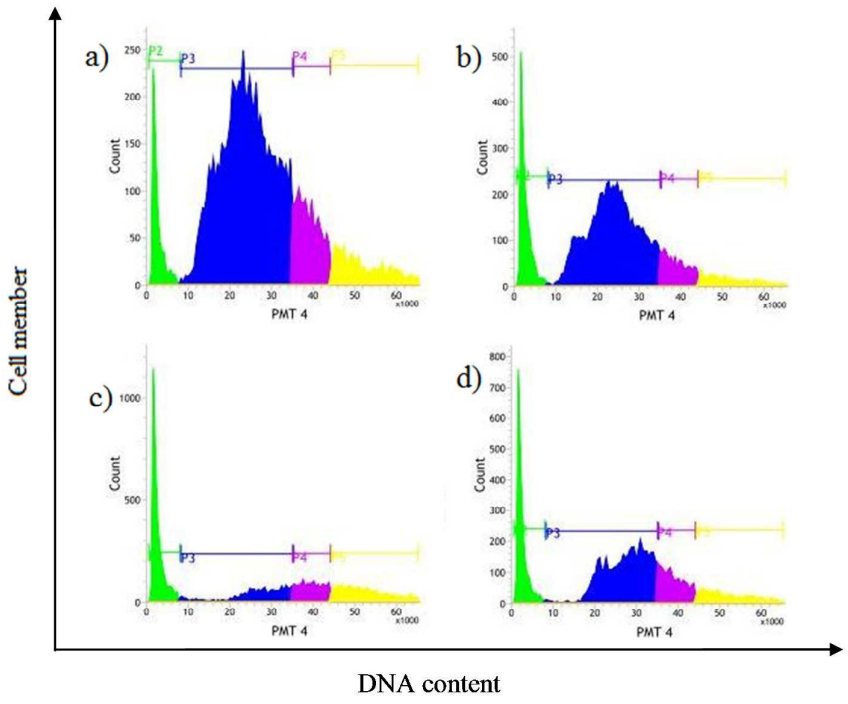

Fig. 11 Effect of MCF-7 control cells (a) and complexes **1** (b), **5** (c), and **6** (d) on cell cycle in MCF-7 cells. Cells were incubated with 25 μM of complexes for 24 h, and their DNA content was analyzed by fluorescence flow cytometry following staining with propidium iodide (PI). P2, P3 and P4 represent G0-G1, S and G2/M phases of cell cycle in the figure, respectively.

G_0-G_1 phase (15.80%, 20.71% and 32.78% for complexes **1**, **5** and **6**, respectively) compared with the control cells (6.62%), accompanied by the corresponding reduction in the percentage of cell population in G_2/M phase were observed. It was noticed that, in S phase, the DNA population decreased (63.56%, 18.34% and 47.16% for **1**, **5** and **6**, respectively) compared with the control cells (68.14%), which suggest antiproliferative mechanism on MCF-7 as S phase arrest and induction of apoptosis [73]. The obtained result is similar to the effect observed with cisplatin (19.3 ± 3.2% in S phase) [74]. Other DNA targeting agents (e.g., 5-fluorouracil) are also known to induce S phase accumulation to prevent DNA-damage-related cell death [75]. Earlier reports have indicated that cisplatin and other platinum agents inhibit cell cycle progression at the G_2/M and S phases [76]. These complexes inhibited MCF-7 cell proliferations as a result of the accumulation of cells in the G_0-G_1 and subsequent reduction in

the G2/M and S phases of the cell cycle, which suggests that complexes **1**, **5** and **6** involves primarily an inhibition of the cellular DNA synthesis leading to a cell cycle.

3. Conclusions

In summary, we have reported the synthesis, spectral characterization and biological evaluation as well as theoretical investigation of a new class of heteroleptic mononuclear copper(II) complexes containing different terpyridines and naproxen drug. The crystal structure of complexes **1** and **6** reveal distorted octahedral geometry around the copper ion involving terpyridine, naproxen and Cl atom. HOMO–LUMO energy gap explains the eventual charge transfer interactions taking place within the molecule. The lowering of HOMO–LUMO band gap supports bioactive property of the molecule. The conductance measurements show that all the metal complexes are non-electrolyte in nature. Electrochemical studies of the complexes display a one electron irreversible transfer waves in the cathodic wave. DNA binding studies of the complexes **1**, **5** and **6** prefer groove mode of binding, and the complexes were also demonstrated to bring about hydrolytic DNA cleavage. The influence of the substituents of the terpyridine ligand was discussed on the basis of computational studies. The pyridine substituent in complex **5** is less hard and more reactive relative to the tolyl and furan substituent of complexes **1** and **6**, respectively. The cytotoxicity of complexes **1**, **5** and **6** on human breast cancer cell line (MCF-7) has been examined. Interestingly, complex **5** exhibit highest antiproliferative activity than that of cisplatin. Analyses of cell configuration and cell cycle revealed with increase in G_0-G_1 and arrest in the S phase, in cell cycle progression for 24 h. The observed results are important towards developing the new heteroleptic complexes of terpyridine and NSAID drug as anticancer agents.

4. Experimental

4.1 Materials

2-Acetyl pyridine, 4-chlorobenzaldehyde, 4-methylbenzaldehyde, 4-dimethylamino benzaldehyde, 3,4-dimethoxybenzaldehyde, 2-furfuraldehyde and 3-pyridinecarboxaldehyde used for ligand synthesis was purchased from AVRA chemicals (India). Solvents of analytical grade were purchased from E. Merck, and used as received without further purification. Tetra(*n*-butyl)ammonium perchlorate (TBAP) used as the supporting electrolyte in the electrochemical measurements was purchased from Fluka (Switzerland). Agarose (molecular biology grade) and ethidium bromide were procured from Sigma-Aldrich (USA). Calf-thymus (CT–DNA) and supercoiled pBR322 DNA were purchased from Bangalore Genei (India). Tris(hydroxymethyl)aminomethane–hydrochloride (Tris–HCl) buffer (pH, 7.3) was used for all DNA binding and cleavage studies.

4.2 Physical measurements

The elemental analysis (CHN) of the compounds was carried out with a Carlo Erba model-1106 elemental analyzer. IR spectra were recorded on the Perkin-Elmer FT/IR 8300 model spectrophotometer using KBr disc technique in the range of 4000–400 cm^{-1}. Electrospray ionization (ESI) mass spectra were recorded on Q-Tof mass spectrometer using acetonitrile as the carrier solvent. Electronic absorption spectra were recorded using Perkin-Elmer Lambda-35 spectrophotometer in the range of 200–800 nm. X-Band EPR spectra of complexes were recorded on Varian EPR-E 112 spectrometer at room temperature. Cyclic voltammograms were obtained on CHI 602D (CH Instruments Co., USA) electrochemical analyzer. The electrochemical workstation was equipped with a three electrode system namely, glassy carbon, platinum wire and Ag/AgCl as working, auxiliary and reference electrodes, respectively. Tetra(*n*-butyl)ammonium perchlorate (TBAP) was used as

supporting electrolyte for the electrochemical work and nitrogen gas was purged prior to all the measurements.

The ligands, 4'-(4-tolyl)-2,2':6',2"-terpyridine (L^1), 4'-(4-dimethylaminophenyl)-2,2':6',2"-terpyridine (L^2), 4'-(3,4-dimethoxyphenyl)-2,2':6',2"-terpyridine (L^3), 4'-(4-chloro phenyl)-2,2':6',2"-terpyridine (L^4), 4'-(pyridin-3-yl)-2,2':6',2"-terpyridine (L^5) and 4'-(furan-2-yl)-2,2':6',2"-terpyridine (L^6) were synthesized by following the procedure describe in the literature [77].

4.3 General procedure for synthesis of heteroleptic copper(II) complexes (1–6)

A methanolic solution of 4′-(4-substituted)-2,2′:6′,2″-terpyridines ($L^{1\text{-}6}$, 1.5 mmol), $CuCl_2.2H_2O$ (0.12 g, 1.5 mmol) and sodium naproxen (0.38 g, 1.5 mmol) was stirred at room temperature for 2 h, and the resulting solution was refluxed for 2 h, filtered hot and kept aside for slow evaporation. The product was washed with diethyl ether and dried in vacuum.

4.3.1 [Cu(L^1)(nap)Cl] (1)

Yield: 0.63 g, (96.6%); Colour: Green; Anal. Calc. for: $C_{36}H_{30}N_3O_3ClCu$ (651.64): C, 66.35; H, 4.64; N, 6.45; Cu, 9.75; Found: C, 66.24; H, 4.32; N, 6.56; Cu, 9.62%. Selected IR data (KBr, υ/cm^{-1}): 3473 υ(O–H str. of MeOH), 1613 υ(C=N), 1564 $\upsilon(COO)_{asy}$, 1377 $\upsilon(COO)_{sym}$. UV-Vis (DMF): λ/nm: 271 (π–π*), 347 (n–π*), 610 (d–d). ESI–MS (m/z): 615.16 [Cu(L^1)(nap)]$^+$. Conductance (Λ_M, Ω^{-1} cm^2 mol^{-1}) in DMF: 18. $g_{\|}$ = 2.09, $g_{\perp}$ = 2.04. μ_{eff} = 1.82 BM.

4.3.2 [Cu(L^2)(nap)Cl] (2)

Yield: 0.62 g, (95.1%); Colour: Greenish brown; Anal. Calc. for: $C_{37}H_{33}N_4O_3ClCu$ (679.15): C, 65.29; H, 4.89; N, 8.23; Cu, 9.34; Found: C, 63.32; H, 4.91; N, 8.29; Cu, 9.39%. Selected IR data (KBr, υ/cm^{-1}): 1618 υ(C=N), 1556 $\upsilon(COO)_{asy}$, 1398 $\upsilon(COO)_{sym}$. UV-Vis (DMF): λ/nm: 265 (π–π*), 342 (n–π*), 601 (d–d). ESI–MS (m/z): 644.18 [Cu(L^2)(nap)]$^+$. Conductance (Λ_M, Ω^{-1} cm^2 mol^{-1}) in DMF: 16. $g_{\|}$ = 2.11, $g_{\perp}$ = 2.06. μ_{eff} = 1.84 BM.

4.3.3 [Cu(L^3)(nap)Cl] (3)

Yield: 0.64 g, (98.2%); Colour: Green; Anal. Calc. for: $C_{37}H_{32}N_3O_5ClCu$ (697.67): C, 63.70; H, 4.62; N, 6.02; Cu, 9.11; Found: C, 63.81; H, 4.54; N, 6.09; Cu, 9.18%. Selected IR data (KBr, υ/cm^{-1}): 1612 υ(C=N), 1562 $\upsilon(COO)_{asy}$, 1378 $\upsilon(COO)_{sym}$. UV-Vis (DMF λ/nm: 272 (π–π*), 358 (n–π*), 612 (d-d). ESI–MS (m/z): 661.16 $[Cu(L^3)(nap)]^+$. Conductance (Λ_M, Ω^{-1} cm^2 mol^{-1}) in DMF: 19. $g_{\|} = 2.14$, $g_{\perp} = 2.07$. $\mu_{eff} = 1.92$ BM.

4.3.4 [Cu(L^4)(nap)Cl] (4)

Yield: 0.61 g, (96.2%); Colour: Green; Anal. Calc. for: $C_{35}H_{27}N_3O_3Cl_2Cu$ (672.06) C, 62.55; H, 4.05; N, 6.25; Cu, 9.46; Found: C, 62.61; H, 3.91; N, 6.20; Cu, 9.51%. Selected IR data (KBr, υ/cm^{-1}): 1611 υ(C=N), 1558 $\upsilon(COO)_{asy}$, 1370 $\upsilon(COO)_{sym}$. UV-Vis (DMF): λ/nm: 276 (π–π*), 343 (n–π*), 620 (d–d). ESI–MS (m/z): 635.10 $[Cu(L^4)(nap)]^+$. Conductance (Λ_M, Ω^{-1} cm^2 mol^{-1}) in DMF: 17. $g_{\|} = 2.12$, $g_{\perp} = 2.06$. $\mu_{eff} = 1.90$ BM.

4.3.5 [Cu(L^5)(nap)Cl] (5)

Yield: 0.58 g, (89.0%); Colour: Green; Anal. Calc. for: $C_{34}H_{27}N_4O_3ClCu$ (638.60) C, 63.95; H, 4.26; N, 8.77; Cu, 9.95; Found: C, 63.98; H, 4.31; N, 8.82; Cu, 9.90%. Selected IR data (KBr, υ/cm^{-1}): 1616 υ(C=N), 1559 $\upsilon(COO)_{asy}$, 1392 $\upsilon(COO)_{sym}$. UV-Vis (DMF): λ/nm: 275 (π–π*), 337 (n–π*), 616 (d–d). ESI–MS (m/z): 602.14 $[Cu(L^5)(nap)]^+$. Conductance (Λ_M, Ω^{-1} cm^2 mol^{-1}) in DMF: 13. $g_{\|} = 2.13$, $g_{\perp} = 2.07$. $\mu_{eff} = 1.86$ BM.

4.3.6 [Cu(L^6)(nap)Cl] (6)

Yield: 0.60 g, (92.0%); Colour: Green; Anal. Calc. for: $C_{33}H_{26}ClCuN_3O_5$ (627.58): C, 63.16; H, 4.18; N, 6.70; Cu, 10.13; Found: C, 63.04; H, 3.86; N, 6.82; Cu, 10.01%. Selected IR data (KBr, υ/cm^{-1}): 3491 υ(O–H str. of CH_3OH/H_2O), 1604, 413 υ(O–H str. of H_2O), 1619 υ(C=N), 1561 $\upsilon(COO)_{asy}$, 1384 $\upsilon(COO)_{sym}$. UV-Vis (DMF): λ/nm: 274 (π–π*), 344 (n–π*), 624 (d–d). ESI–MS (m/z): 592.12 $[Cu(L^6)(nap)]^+$. Conductance (Λ_M, Ω^{-1} cm^2 mol^{-1}) in DMF: 17. $g_{\|} = 2.10$, $g_{\perp} = 2.05$. $\mu_{eff} = 1.93$ BM.

4.4 Crystal structure determination

Single crystals of complexes **1** and **6** were grown by slow evaporation from methanol. Single crystals with dimension of 0.30×0.25×0.20 and 0.30×0.20×0.20 mm for complexes **1** and **6,** respectively, were mounted on glass fibre with epoxy cement for diffraction experiment. All geometric and intensity data were collected using an automated Bruker SMART APEX CCD diffractometer equipped with a fine focus 1.75 kW sealed tube, Mo-Kα X-ray source (λ = 0.71073 Å) with increasing ω (width of 0.3° per frame) at a scan speed of 5 s per frame. The intensity data were corrected for the Lorentz polarization as well as for absorption effects. The crystal structures were solved by direct methods (SHELXS–97) and refined against F^2 by full-matrix least-squares methods using all data (SHELXL–2012) [78].

4.5 Computational details

The molecular structure of the complexes **1** and **6** in the ground state was optimized by a DFT method using B3LYP functional [79, 80] combined with 6-31G(d) and LANL2DZ basis sets. Calculations were carried out using Gaussian 03 software [81].

4.6 DNA binding studies

4.6.1 Absorption spectral titration

Electronic absorption spectroscopy is employed to examine the binding mode of CT–DNA with small molecules. The UV absorbance at 260 and 280 nm of the CT–DNA in 5 mM Tris–HCl/50 mM NaCl buffer (pH, 7.3) solution at room temperature gave a ratio of 1.8-1.9:1, indicating that the DNA was sufficiently free from proteins [82]. Stock solutions of CT–DNA was prepared in Tris–HCl/NaCl buffer and stored at 4 ºC for less than 4 days. The concentration of DNA in nucleotide phosphate was determined by UV absorbance at 260 nm. The molar absorption coefficient of CT–DNA was taken as 6600 $M^{-1}cm^{-1}$. Absorption titration experiments were performed by maintaining the constant complex concentration (25 μM) and varying the concentration of the CT–DNA (0−5.0 μM). Complex–DNA

solutions were allowed to incubate for 30 min at room temperature before measurements were taken. While measuring the absorption spectra, equal quantity of CT–DNA was added to both the complex solution and reference solution to eliminate the absorbance of CT–DNA itself. The intrinsic binding constants, K_b can be obtained by the following equation:

$$[DNA]/(\varepsilon_a - \varepsilon_f) = [DNA]/(\varepsilon_b - \varepsilon_f) + 1/K_b\,(\varepsilon_b - \varepsilon_f)$$

where ε_a, ε_f, and ε_b correspond to A_{obsd}/[complex], the extinction coefficient for the free copper complex, and the extinction coefficient for the copper complex in the fully bound form, respectively. A plot of $[DNA]/(\varepsilon_a - \varepsilon_f)$ *versus* [DNA] gives K_b as the ratio of the slope to the intercept.

4.6.2 DNA melting experiments

DNA melting experiments were carried out by monitoring the absorption (260 nm) of CT–DNA (100 μM) at various temperatures in the absence and presence of complexes (25 μM). The melting temperature T_m was calculated by plotting temperature *versus* relative absorption intensity (A/A_0), and measurements were carried out using a Perkin–Elmer Lambda 35 spectrophotometer equipped with a Peltier temperature controlling programmer (PTP 6) (±0.1 °C) on increasing the temperature of the solution by 0.5 °C per min.

4.6.3 Viscosity measurements

Viscometric experiments were carried out using an Ostwald–type viscometer of 2 mL capacity, thermostated in a water bath maintained at 25 ± 1 ºC. DNA (20 μM) and DNA with the copper complexes at various concentrations (0–100 μM) were prepared by using Tris–HCl/NaCl buffer (pH = 7.3). Mixing of the solution was achieved by purging nitrogen gas through viscometer. The flow times were measured with a digital timer, and each sample was measured three times for accuracy, and an average flow time was calculated. Data are presented as η/η_0 *vs*. 1/R, where η is the relative viscosity of DNA in the presence of the copper(II) complex and η_0 is the relative viscosity of DNA alone. The viscosity values were

calculated from the observed flow time of the solutions containing DNA (t) and corrected for that of the buffer alone (t_b), using the following equation [83]:

$$\eta = (t - t_b)/t_b$$

4.6.4 Electrochemical titration

The electrochemical investigation of metal–DNA interaction may be a useful supplement to spectroscopic methods and provide information about interaction with both the reduced and oxidized form of the metal. Double distilled water was used to prepare the buffer solutions. The solutions of complexes and DNA were prepared by using DMF and Tris–HCl/NaCl buffer (pH 7.3), respectively. The concentration of complexes can be taken as 100 μM and also for DNA. Solutions were deoxygenated by purging with N_2 prior to measurements.

4.6.5 Molecular docking studies

Molecular docking studies were carried out using the AutoDock Tools (ADT) version 1.5.6 and AutoDock version 4.2.5.1 docking programmes. Structure of the complexes **1**, **5** and **6** was converted into PDB format from mol format by OPENBABEL. The crystal structure of the B–DNA dodecamer d(CGCGAATTCGCG)$_2$ (PDB ID: 1BNA) was downloaded from the protein data bank (http://www.rcsb.org./pdb). Receptor (DNA) and ligand (complexes) files were prepared using AutoDock Tools. First, all the heteroatoms including water molecules were deleted and polar hydrogen atoms and Kollman charges were added to receptor molecule, then rotatable bonds in ligands were assigned. All other bonds were allowed to rotate. The DNA was enclosed in a box with number of grid points in x × y × z directions, 60 × 60 × 110 and a grid spacing of 0.375 Å. Lamarckian genetic algorithms, as implemented in AutoDock, were employed to perform docking calculations. All other parameters were default settings. For each of the docking cases, the lowest energy docked conformation, according to the Autodock scoring function, was selected as the binding mode. Visualization

of the docked position has been done by using CHIMERA (www.cgl.ucsf.edu/chimera) molecular graphics program.

4.7 Gel electrophoresis

Cleavage of DNA by the synthesized copper(II) complexes was monitored by using the agarose gel electrophoresis technique by determining their ability to convert supercoiled DNA (Form I) to open circular (Form II) and linear (Form III) forms. In the cleavage experiments, the plasmid pBR322 DNA (33.3 μM) was treated with different concentration of complexes. The samples were incubated at 37 ºC for 1 h, a loading buffer containing 25% bromophenol blue, 0.25% xylene cyanol, 30% glycerol was added and electrophoresis was performed at 50 V for 1 h in TAE buffer using 0.8% agarose gel containing 1.0 mg/mL ethidium bromide, and was photographed on UV illuminator. The degree of DNA cleavage activity was expressed in terms of the percentage of conversion of the SC DNA to NC DNA according to the following equation:

$$\text{DNA cleavage activity (\%)} = \frac{(\%\ \text{of SC DNA})_{\text{control}} - (\%\ \text{of SC DNA})_{\text{sample}}}{(\%\ \text{of SC DNA})_{\text{control}}} \times 100$$

For relegation experiments, the NC DNA was recovered from agarose gel by phenol extraction method and purified by ethanol precipitation. Subsequently, the purified NC DNA was incubated with T4 DNA ligase in a 10× ligation buffer for 16 h at 25 °C and subjected to gel electrophoresis.

4.8 Cell proliferation assay

4.8.1 Cell lines

MCF-7 (Breast cancer) cell line was obtained from National Centre for Cell Science (NCCS), Pune, India, and cultured in Dulbecco's Modified Eagles Medium (DMEM) (St. Louis, Mo, USA), The medium was supplemented with 10% heat inactivated Fetal Bovine Serum (FBS), penicillin 100 μg/mL, streptomycin 20 μg/mL, Kanamycin acid sulphate

20 μg/mL and 7.5% sodium bicarbonate solution. The cell lines were maintained at 37 °C in a 5% CO_2 incubator and the media were changed frequently. MTT [3-(4,5-dimethylthiazol-2-yl)-2,5-diphenyltetrazolium bromide, a yellow tetrazole] was obtained from Himedia, India.

4.8.2 MTT assay

The cytotoxic effect of complexes **1**, **5** and **6** on MCF-7 cells was determined by MTT assay as described by Mosmann [84]. The MCF-7 cells were grown in DMEM medium containing 10% FBS. For screening experiments, the cells (5×10^3 cells/well) were plated in 96-well plates with the medium containing 10% FBS and incubated for 24 h under CO_2 at 37 ºC. Later, the medium was replaced with DMEM containing 1% FBS and the complexes **1**, **5** and **6** (50, 25, 10, 5 and 2 μM) dissolved in 0.1% DMSO were added to the cells incubated at 37 ºC in 5% CO_2. After treatment, the plates were incubated for 24 h in order to perform cytotoxic analysis using MTT assay. MTT was prepared at a concentration of 5 mg/mL and 10 μL of MTT was added to each well and incubated for 4 h. Purple color farmazone crystals formed were then dissolved in 100 μL of dimethylsulfoxide (DMSO). These crystals were observed at 570 nm in a multi well ELISA plate reader. The % of cell viability was evaluated using the following equation:

$$\text{Cell viability (\%)} = \frac{A_{570\ \text{nm}} \text{ of treated cells}}{A_{570\ \text{nm}} \text{ of control cells}} \times 100$$

4.8.3 Hoechst staining and photomicroscopy

To analyze the morphological apoptotic changes, 1×10^5 MCF-7 (Human Breast Cancer Cells) cells seeded in 96-well plates (37 °C, 5% CO_2), when logarithmic growth phase of cells was reached, the test compounds with various concentrations or 0.1% DMSO (negative control) was added. After 48 h, the cells were washed in phosphate-buffered saline (PBS) and stained for 10 min at room temperature in PBS containing 40% paraformaldehyde and 10 mg/mL Hoechst 33258. MCF-7 cells for Hoechst staining were grown on sterilized cover slips and processed as described with modifications [85]. Briefly, after washing one

time with PBS, cells were fixed with 3.7% formaldehyde in PBS for 10 min, washed one time with PBS, stained with 0.4 mg/mL Hoechst (Molecular Probes, Eugene, USA) in PBS for 15 min, washed two times with PBS, and then one time with water. Cover slips were then air-dried and mounted with Slow Fade (Molecular Probes) mounting media. Morphological evaluations of nuclear condensation and fragmentation were performed immediately after staining by means of fluorescent microscope (Olympus, Japan) at 550 nm of emission.

4.8.4 Flow cytometry

4.8.4.1 Apoptosis analysis

The apoptotic evaluation was also carried out using flow cytometer. MCF-7 cells (5×10^5) were seeded into 6 well plates in Dulbecco's modified Eagle medium (DMEM) containing 10% FBS. After 24 h of incubation at 37 °C in a CO_2 incubator, 0.1% DMSO solutions of complexes **1** (25 μM), **5** (25 μM), and **6** (25 μM) were added to the cells, and incubation was continued in the dark for 1 h. The medium was subsequently replaced with DPBS and irradiation was performed for 1 h with visible light (400–700 nm) using a Luzchem Photoreactor. After irradiation, DPBS was removed and replaced with DMEM containing 10% FBS and incubation was continued in the dark for a further period of 24 h. The cells were trypsinized, washed twice with PBS, and suspended in 500 μL of PBS for 15 min on ice. The cell suspension was mixed with 5 mL of cold 70% ethanol and stored at 4 °C until analysis. On the day of analysis, cells were washed twice with PBS buffer and re-suspended in 1 mL PBS. After incubation with RNase A (250 μg/mL) for 30 min and staining with propidium iodide (PI, 10 μg/mL) for 10 min, flow cytometric analysis was performed using a FACScan fluorescence-activated cell sorter (Becton Dickinson (BD) cell analyzer) at the FL2 channel (595 nm) and the distribution of cell in various cell cycle phases was determined from the histogram generated by "Cell Quest Pro" software (BD Biosciences, San Jose, CA, USA) [86].

4.8.4.2 Cell cycle analysis

To determine the effect of complexes **1**, **5** and **6** on the cell cycle, cells were seeded in 6-well plates at a density of 5×10^5 cells/mL for 24 h. The cells were treated with the IC_{50} concentration of the complexes. The cells were trypsinized, washed twice with PBS, and suspended in 500 µL of PBS for 15 min on ice. The cell suspension was mixed with 5 mL of cold 70% ethanol and stored at 4 °C until analysis. On the day of analysis, cells were washed twice with PBS buffer and re-suspended in 1 mL PBS. After incubation with RNase A (250 µg/mL) for 30 min and staining with propidium iodide (PI, 10 µg/mL) for 10 min, cell cycle analysis was carried out using the FACScan fluorescence-activated cell sorter (Becton Dickinson (BD) cell analyzer) at the FL2 channel (595 nm) and the distribution of cell in various cell cycle phases was determined from the histogram generated by "Cell Quest Pro" software (BD Biosciences, San Jose, CA, USA)

Supplementary material

Electronic supplementary information (ESI) available. CCDC 1021393 and 1033741 contains the supplementary crystallographic data for complexes **1** and **6**, respectively. These data can be obtained free of charge from http://www.ccdc.cam.ac.uk/conts/retrieving.html or from the CCDC (12 Union Road, Cambbridge CB2 1EZ, UK; Fax: +44-1223-336033; e-mail: deposit@ccdc.cam.ac.uk).

Acknowledgements

We are thankful to Tamil Nadu Veterinary and Animal Sciences University, Chennai-600 007, for *in vitro* anticancer studies. We are also thankful to Dr. Rajamony Jagan, SAIF, Indian Institute of Technology-Madras, Chennai-600 036, for his help in solving crystal structure. Help rendered by A. Vishwanadhan CAS in Crystallography and Bioinformatics, University of Madras, Chennai-600 025, towards XRD data collection is greatly acknowledged.

References

1. F. Cisnetti and A. Gautier, *Angew. Chem. Int. Ed.* 2013, **52**, 11976–11978.
2. M. Magnarin, A. Bergamo, M. E. Carotenuto, S. Zorzet and G. Sava, *Anticancer. Res.* 2000, **20**, 2939–2944.
3. J. D. Ranford, P. J. Sadler and D. A. Tocher, *J. Chem. Soc. Dalton Trans.* 1993, 3393–3399.
4. L. M. Mirica, X. Ottenwaelder and T. D. P. Stack, *Chem. Rev.* 2004, **104**, 1013–1046.
5. M. L. P. D. Santos, A. F. Alario, A. S. A. Mangrich and A. M. C. Ferreira, *J. Inorg. Biochem.* 1998, **71**, 71–78.
6. R. Senthil Kumar and S. Arunachalam, *Polyhedron* 2007, **26**, 3255–3262.
7. A. Robert and B. Meunier, *Chem. Eur. J.* 1998, **7**, 1287–1296.
8. C. D. Fan, H. Su, J. Zhao, B. X. Zhao, S. L. Zhang and J. Y. Miao, *Eur. J. Med. Chem*. 2010, **45**, 1438–1446.
9. J. P. Sauvage, J. P. Collin, J. C. Chambron, S. Guillerez, C. Coudret, V. Balzani, F. Barigelletti, L. D. Cola and L. Flamigni, *Chem. Rev*. 1994, **94**, 993–1019.
10. G. Chelucci, A. Saba,F. Soccolini and D. Vignola,*J. Mol. Cat. A: Chem*. 2002, **178**, 27–33.
11. A. Kumar, J. P. Chinta, A.K. Ajay, M.K. Bhat and C.P. Rao, *Dalton Trans*. 2011, **40**, 10865–10872
12. D. J. A. de Groot, E. J. E. de Vries, H. J. M. Groen and S. de Jong, *Crit. Rev. Oncol. Hematol.* 2007, **61**, 52–69.
13. R. T. Schoen and R. Vender, *J. Am. J. Med*. 1989, **86**, 449–458.
14. J. R. Sorenson, *Prog. Med. Chem*. 1989, **26**, 437–568.
15. S. Rajalakshmi, T. Weyhermuller, A. J. Freddy, H. R. Vasanthi and B. U. Nair, *Eur. J. Med. Chem*. 2011, **46**, 608–617.
16. F. Dimiza, F. Perdih, V. Tangoulis, I. Turel, D. P. Kessissoglou and G. Psomas, J. Inorg. Biochem. 2011, 105, 476–489.
17. A.L. Abuhijleh and J. Khalaf, Eur. J. Med. Chem. 2010, 45, 3811–3817.
18. C. Dendrinou-Samara, G. Tsotsou, C. P. Raptopoulou, A. Kortsaris, D. Kyriakidis and D. P. Kessissoglou, *J. Inorg. Biochem*. 1998, **71**, 171–179.
19. M. Lee, A. L. Rhodes, M. D. Wyatt, S. Forrow and J. A. Hartley, *Biochemistry* 1993, **32**, 4237–4245.
20. M. N. Patel, H. N. Joshi and B. S. Bhatt, *Polyhedron* 2010, **29**, 3238–3245.
21. P. Kubelka and F. Munk, *Tech. Z. Phys*. 1931, **12**, 593–601.
22. D. F. V. Lewis, C. Ioannides and D. V. Parke, *Xenobiotica*, 1994, **24**, 401–408.

23. J. Li, J. C. Chen, L. C. Xu, K. C. Zheng and L. N. Ji, *J. Organomet. Chem*. 2007, **692**, 831–838.
24. M. Bose, K. Ohta, Y. Babu and M. D. Sastry, *Chem. Phys. Lett*. 2000, **324**, 330–336.
25. M. Shebl, *J. Coord. Chem*. 2009, **62**, 3217–3231.
26. W. J. Geary, *Coord. Chem. Rev*. 1971, **7**, 81–122.
27. R. H. Fish and G. Jaouen, *Organometallics.* 2003, **22**, 2166–2177.
28. H. L. Chan, Q. L. Liu, B. C. Tzeng, Y. S. You, S. M. Peng, M. Yang and C. M. Che, *Inorg. Chem*. 2002, **41**, 3161–3171.
29. D. R. McMillan and K. M. McNett, *Chem. Rev*. 1998, **98**, 1201–1220.
30. V. M. Manikandamathavan, T. Weyhermüller, R. P. Parameswari, M. Sathishkumar, V. Subramanian and B. U. Nair, *Dalton Trans.* 2014, **43**, 13018–13031.
31. S. Rajalakshmi, M. S. Kiran and B. U. Nair, *Eur. J. Med. Chem.* 2014, **80**, 393–406.
32. V. Uma, M. Elango and B. U. Nair, *Eur. J. Inorg. Chem.* 2007, 3484–3490.
33. F. Dimiza, A.N. Papadopoulos, V. Tangoulis, V. Psycharis, C.P. Raptopoulou, D.P. Kessissoglou and G. Psomas, *J. Inorg. Biochem*. 2012, **107**, 54–64
34. F. Arjmand, F. Sayeed and D. Muddassir, *J. Photochem. Photobiol. B*: 2011, **103**, 166–179.
35. M. Cory, D. D. Mckee, J. Kagan, D. W. Henry and J. A. Miller, *J. Am. Chem. Soc*. 1985, **107**, 2528–2536.
36. G. L. Eichhorn and Y. A. Shin, *J. Am. Chem. Soc*. 1968, **90**, 7323–7328.
37. L. Lerman, *J. Mol. Biol*. 1961, **3**, 18–30.
38. M. Roy, T. Bowmick, R. Santhanagopal, S. Ramakumar and A. R. Chakravarty, *Dalton Trans*. 2009, 4671–4682.
39. F. Dimiza, A. N. Papadopoulos, V. Tangoulis, V. Psycharis, C. R. Raptopoulou, D. P. Kessissoglou and G. Psomas, *Dalton Trans*. 2010, **39**, 4517–4528.
40. Y. Fei, G. Lu, G. Fan and Y. Wu, *Anal. Sci*. 2009, **25**, 1333–1338.
41. M. Chikira, S. Suda, T. Nakabayashi, Y. Fujiwara, T. Ejiri, M. Yoshikawa, N. Kobayashi and H. Shindo, *J. Chem. Soc., Dalton Trans*. 1995, 1325–1331.
42. V.C. da Silveira, H. Benezra, J.S. Luz, R.C. Georg, C.C. Oliveira and A.M. da Costa Ferreira, *J. Inorg. Biochem*. 2011, **105**, 1692–1703.
43. R. Filosa, A. Peduto, S. D. Micco, P. De Caprariis, M. Festa, A. Petrella, G. Capranico and G. Bifulco, *Bioorg. Med. Chem*. 2009, **17**, 13–24.
44. R. Corradini, S. Sforza, T. Tedeshi and R. Marchelli, *Chirality*. 2007, **19**, 269–294.
45. P. Yang and M. Guo, *Met.-Based Drugs*. 1998, **5**, 41–58.

46. R. G. Parr and P. K. Chattaraj, *J. Am. Chem. Soc*. 1991, **113**, 1854−1855.

47. P. V. R. Schleyer, C. Maerker, A. Dransfeld, H. Jiao and N. J. R. V. E. Hommes, *J. Am. Chem. Soc*. 1996, **118**, 6317–6318.

48. J. K. K. Bania and R. C. Deka, *Phys. Chem. C*. 2012, **116**, 14295–14310.

49. G. Parkin, *Chem. Rev*. 2004, **104**, 699–767.

50. V. M. Manikandamathavan, R. P. Parameswari, T. Weyhermüller, H. R. Vasanthi and B. U. Nair, *Eur. J. Med. Chem.* 2011, **46**, 4537–4547.

51. S. Dhar, P. A. N. Reddy and A. R. Chakravarty, *Dalton Trans.* 2004, 697–698.

52. F. V. Pamatong, C. A. Detmer III and J. R. Bocarsly, *J. Am. Chem. Soc.* 1996, **18**, 5339–5345.

53. X. Gao, Y. Lu, L. Fang, X. Fang, Y. Xing, S. Gou and T. Xi, *Eur. J. Med. Chem*. 2013, **69**, 1–9.

54. U. V. Mallavadhani, N. R. Vanga, M. K. Jeengar and V. G. M. Naidu, *Eur. J. Med. Chem*. 2014, **74**, 398–404.

55. B. Banik, K. Somyajit, G. Nagaraju and A.R. Chakravarty, *Dalton Trans.* 2014, **43**, 13358–13369

56. B. Balaji, B. Balakrishnan, S. Perumalla, A.A. Karande and A.R. Chakravarty, *Eur. J. Med. Chem.* 2015, **92**,332–341.

57. P. Kumar, S. Gorai, M.K. Santra, B. Mondal and D. Manna, *Dalton Trans.* 2012, **41**, 7573–7581

58. G. Hacker and S. A. Paschen, *Expert. Opin. Ther. Targets.* 2007, **11**, 515–526.

59. M. D. Jacobson, M. Weil and M. C. Raff, *Cell* 1997, **88**, 347–354.

60. E. White, *Genes Dev.* 1996, **10**, 1–15.

61. J. F. Kerr, A. H. Wyllie and A. R. Currie, *Br. J. Cancer* 1972, **26**, 239–257.

62. A. H. Wyllie. *Cancer Metast Rev.* 1992, **11**, 95–103.

63. J. F. Kerr, C. M. Winterford and B. V. Harmon, *Cancer* 1994, **73**, 2013–2026.

64. N. Itoh, S. Yonehara, A. lshii, M. Yonehara, S. Mizushima, M. Sameshima, A. Hase, Y. Seto and S. Nagata, *Cell* 1991, **66**, 233–243.

65. D. E. Fisher, *Cell.* 1994, **78**, 539–542.

66. G. Majno and I. Joris, *Am. J. Pathol.* 1995, **146**, 3–15.

67. D. Martin, M. Lenardo, J. E. Coligen, A. M. Kruisbeek, D. H. Margulies, E. M. Shevach and W. S. Strober, eds. John Wiley & Sons, New York. 1998, 3.17.1–3.17.39.

68. S. A. Boehme and M. J. Lenardo. *Eur. J. Immunol.* 1993, **23**, 1552–1560.

69. J. M. Critchfield, M. K. Racke, J. C. Zuniga-Pflucker, B. Cannella, C. S. Raine, J. Goverman and M. J. Lenardo. *Science* 1994, **263**, 1139–1143.

70. K. Mitra, U. Basu, I. Khan, B. Maity, P. Kondaiah and A. R. Chakravarty, *Dalton Trans.* 2014, **43**, 751–763

71. D. Tao, J. Wu, Y. Feng, J. Qin, J. Hu and J. Gong, *Cytometry Part A.* 2004, **57**, 70–74.

72. W. G. Telford, L. E. King and P. Fraker. *J. Immunol. Methods.* 1994, **172**, 1–16.

73. Q. Wu, C. Fan, T. Chen, C. Liu, W. Mei, S. Chen, B. Wang, Y. Chen and W. Zheng, *Eur. J. Med. Chem.* 2013, **63**, 57–63.

74. N. Yamane, M. Makino and N. Kaibara, *Cancer* 1999, **85**, 309–317.

75. K. Suntharalingam, D. J. Hunt, A. Duarte, A. J. P. White and D. J. Mann, R. Vilar, *Chem. Eur. J.* 2012, **18**, 15133–15141

76. Z. H. Siddik, *Oncogene* 2003, **22**, 7265–7279.

77. J. Wang and G. S. Hanan, *Synlett*. 2005, **8**, 1251–1254.

78. G.M. Sheldrick, *Crystallogr. Sect. A* 2008, **64**, 112−122.

79. M. J. Frisch, G. W. Trucks, H. B. H. Schlegel, G. E. Scuseria, M. A. Robb, J. R. Cheeseman, V. G. Zakrzewski, J. A. Montgomery, R. E. Stratmann, J. C. Burant, S. Dapprich, J.M. Millam, A. D. Daniels, K. N. Kudin, M. C. Strain, O. Farkas, J. Tomasi, V. Barone, M. Cossi, R. Cammi, B. Mennucci, C. Pomelli, C. Adamo, S. Clifford, J. Ochterski, G. A. Petersson, P. Y. Ayala, Q. Cui, K. Morokuma, D. K. Malick, A. D. Rabuck, K. Raghavachari, J. B. Foresman, J. Cioslowski, J. V. Ortiz, A. G. Baboul, B. B. Stefanov, G. Liu, A. Liashenko, P. Piskorz, I. Komaromi, R. Gomperts, R. L. Martin, D. J. Fox, T. Keith, M. A. Al-Laham, C. Y. Peng, A. Nanayakkara, C. Gonzalez, M. Challacombe, P. M. W. Gill, B. G. Johnson, W. Chen, M. W. Wong, J. L. Andres, M. Head-Gordon, E. S. Replogle and J. A. Pople, Gaussian 03 (Revision A.9), Gaussian, Inc., Pittsburgh, 2003.

80. A. D. Becke, *J. Chem. Phys*. 1993, **98**, 5648–5652.

81. C. Lee, W. Yang and R. G. Parr, *Phys. Rev. B*. 1988, **37**, 785–789.

82. J. Marmur, *J. Mol. Biol*. 1961, **3**, 208–218.

83. A. I. Huguet, S. Manez and M. J. Alcaraz, *Z. Naturforsch* 1990, **45**, 19–24.

84. T. Mosmann, *J. Immuno. Methods*. 1983, **65**, 55–63.

85. R. Bergan, E. Kyle, P. Nguyen, J. Trepel and L. Neckers. *Clin. Exp. Metastasis*. 1996, **14**, 389–398.

86. A. Roy, M. S. Singh, P. Upadhyay and S. Bhaskar, *Mol. Pharm*. 2010, **7**, 1778–1788.